TOI-332 b: a super dense Neptune found deep within the Neptunian desert

Ares Osborn,[1,2],[★] David J. Armstrong[1,2], Jorge Fernández Fernández[1,2], Henrik Knierim[3],
Vardan Adibekyan[4], Karen A. Collins[5], Elisa Delgado-Mena[4], Malcolm Fridlund[6], João Gomes da Silva[4],
Coel Hellier[7], David G. Jackson[8], George W. King[9,1,2], Jorge Lillo-Box[10], Rachel A. Matson[11],
Elisabeth C. Matthews[12], Nuno C. Santos[4,13], Sérgio G. Sousa[4], Keivan G. Stassun[14], Thiam-Guan Tan[15],
George R. Ricker[16], Roland Vanderspek[16], David W. Latham[5], Sara Seager[16,17,18], Joshua N. Winn[19],
Jon M. Jenkins[20], Daniel Bayliss[1,2], Luke G. Bouma[21], David R. Ciardi[22], Kevin I. Collins[23],
Knicole D. Colón[24], Ian J. M. Crossfield[16], Olivier D. S. Demangeon[4,13], Rodrigo F. Díaz[25],
Caroline Dorn[26], Xavier Dumusque[27], Marcelo Aron Fetzner Keniger[1,2], Pedro Figueira[27,4], Tianjun Gan[28],
Robert F. Goeke[16], Andreas Hadjigeorghiou[1,2], Faith Hawthorn[1,2], Ravit Helled[3], Steve B. Howell[20],
Louise D. Nielsen[29], Hugh P. Osborn[30], Samuel N. Quinn[5], Ramotholo Sefako[31], Avi Shporer[16],
Paul A. Strøm[1,2], Joseph D. Twicken[32,20], Andrew Vanderburg[16], and Peter J. Wheatley[1,2]
The authors' affiliations are shown in Appendix F.

ABSTRACT

To date, thousands of planets have been discovered, but there are regions of the orbital parameter space that are still bare. An example is the short period and intermediate mass/radius space known as the "Neptunian desert", where planets should be easy to find but discoveries remain few. This suggests unusual formation and evolution processes are responsible for the planets residing here. We present the discovery of TOI-332 b, a planet with an ultra-short period of 0.78 d that sits firmly within the desert. It orbits a K0 dwarf with an effective temperature of 5251 ± 71 K. TOI-332 b has a radius of $3.20^{+0.16}_{-0.12}$ $R_\oplus$, smaller than that of Neptune, but an unusually large mass of 57.2 ± 1.6 $M_\oplus$. It has one of the highest densities of any Neptune-sized planet discovered thus far at $9.6^{+1.1}_{-1.3}$ g cm^{-3}. A 4-layer internal structure model indicates it likely has a negligible hydrogen-helium envelope, something only found for a small handful of planets this massive, and so TOI-332 b presents an interesting challenge to planetary formation theories. We find that photoevaporation cannot account for the mass loss required to strip this planet of the Jupiter-like envelope it would have been expected to accrete. We need to look towards other scenarios, such as high-eccentricity migration, giant impacts, or gap opening in the protoplanetary disc, to try and explain this unusual discovery.

Key words: exoplanets – planets and satellites: detection – planets and satellites: individual: (TOI-332, TIC 139285832)

1 INTRODUCTION

One of the key outcomes of the *Kepler* mission (Borucki et al. 2010) was the population studies performed on the planets it discovered. This led to the identification of the "Neptunian desert" (also known as the "hot Neptune desert", "sub-Jovian desert", and "evaporation desert"), a region of period-radius and period-mass parameter space where planets have, so far, been rarely found. The desert was first noted by Szabó & Kiss (2011), and has been the subject of many studies in the years since (e.g., Boué et al. 2012; Beaugé & Nesvorný 2013; Helled et al. 2016; Lundkvist et al. 2016), and its boundaries were first formally defined by Mazeh et al. (2016). As shown in Fig. 1, it is a wedge shaped region where the upper boundary at large radii (or mass) decreases with increasing semi-major axis, and a lower boundary at small radii (or mass) which increases with increasing

semi-major axis. The desert roughly encompasses intermediately-sized planets (approximately $2 R_\oplus < R_P < 9 R_\oplus$ and $10 M_\oplus < M_P < 250 M_\oplus$) with periods out to ~ 5 days.

This should not be due to an observational bias, as Neptune-sized planets with short periods are readily discovered by transit surveys like *Kepler* and, more recently, the Transiting Exoplanet Survey Satellite (*TESS*, Ricker et al. 2015). Theories have been put forward to explain the desert's existence and boundaries (e.g., Owen & Lai 2018; Vissapragada et al. 2022). The lower boundary could be caused by photoevaporation of planets above the boundary, stripping their envelopes and reducing their radii/mass; while the upper boundary seems to be stable against photoevaporation, and may instead be understood as a "tidal disruption barrier", where planets below and left of the boundary migrating inwards can no longer successfully circularise and stabilise (see review by Dawson & Johnson (2018)).

In the years since its discovery, the desert has become more populated with planet discoveries, especially around its boundaries. How-
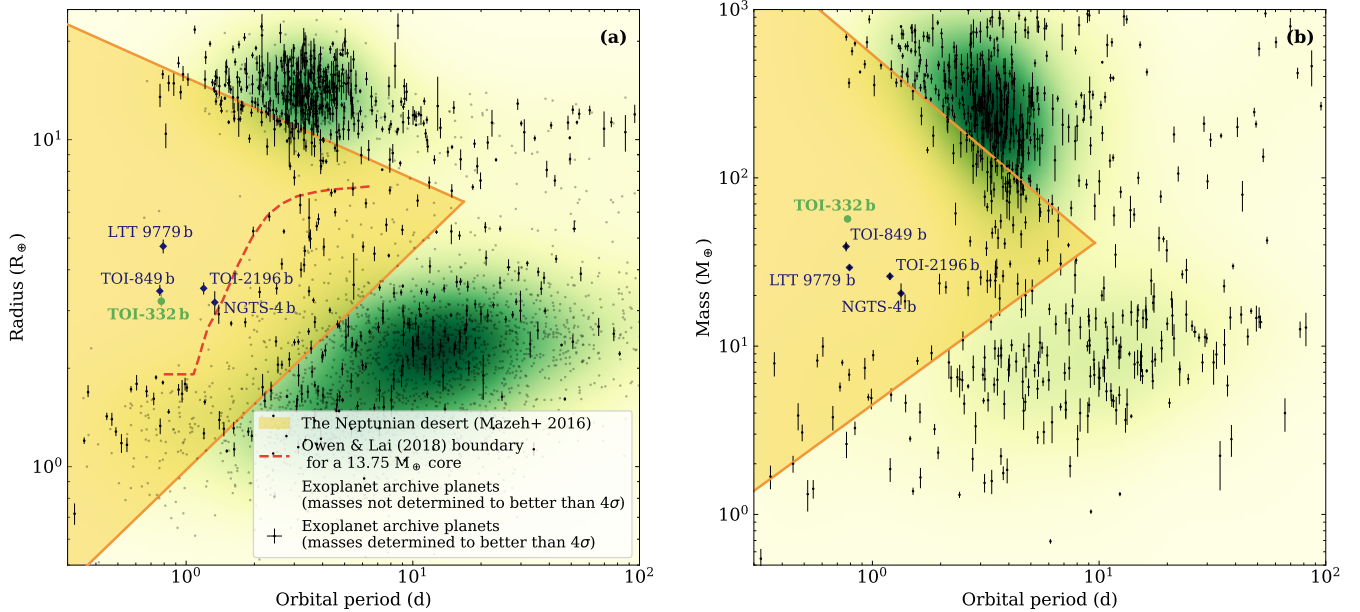
Figure 1. TOI-332 b (green circle) in the context of the Neptunian desert, with **(a)** showing period-radius space, and **(b)** showing period-mass. The Neptunian desert boundaries from Mazeh et al. (2016) are plotted as solid lines, with the enclosed Neptunian desert area shaded in yellow. In **(a)**, the dashed line is a numerical solution for the lower boundary of the desert determined for a 13.75 $M_\oplus$ core in Owen & Lai (2018). Known planets were sourced from the NASA exoplanet archive (https://exoplanetarchive.ipac.caltech.edu/) on 3 May 2023: those without mass determinations or mass determinations worse than 4 σ are plotted as pale grey dots in **(a)** only; planets with mass determinations better than 4 σ are plotted as black dots in both **(a)** and **(b)**. Population density of known planets is shaded in green, where darker green denotes more planets discovered in that region of parameter space: in **(a)** this includes all planets; in **(b)** this includes only planets with mass determination better than 4 σ. Particular planets with mass determination to better than 4 σ that are considered to be in the "deep" Neptunian desert are labelled (dark blue diamonds).

ever, there are so far only four planets with precisely determined masses (i.e. an error on their mass of better than 20 per cent) found deep within the desert, far from the boundaries set by Mazeh et al. (2016): NGTS-4 b (West et al. 2019); LTT-9779 b (Jenkins et al. 2020); TOI-849 b (Armstrong et al. 2020); and TOI-2196 b (Persson et al. 2022). They are annotated in Fig. 1. There are an additional few without precise masses: K2-100 b (Barragán et al. 2019); K2-278 b (Livingston et al. 2018), and Kepler-644 b (Morton et al. 2016), the latter two being validated and having no mass determination. The few planets found in this barren desert are likely to have undergone unusual formation and/or evolutionary processes compared to those in more populated parameter spaces. There are now concerted efforts to find planets in and around the desert (e.g. Magliano et al. 2023; Bourrier et al. 2023) to determine what sculpts it.

The aim of the HARPS-NOMADS program is to characterise planets in the Neptunian desert discovered by *TESS*, as the stars it observes are bright enough for effective radial velocity follow up. By precisely determining their masses and radii, we can constrain densities and thus the internal structures of these planets in order to understand their formation and evolution, leading to a better understanding of the origins of the desert itself.

We present here the detection and characterisation of TOI-332 b, an ultra-short period planet with an unusually high density located deep within the Neptunian desert. In Section 2, we present the observations of the TOI-332 system, including photometry, spectroscopy, and high-resolution imaging. The spectroscopic analysis and derivation of chemical abundances of the star is then described in Section 3. In Section 4, we describe the joint fit model to the data. In Section 5, we present the results of the joint fit, discuss the nature of TOI-332 b, theorise potential scenarios for its formation and evolution, and out-

Table 1. Details for the TOI-332 system.

Property	(unit)	Value	Source
Identifiers			
TIC ID		139285832	TICv8
2MASS ID		J23121409-4452349	2MASS
Gaia ID		6529471108882243840	Gaia DR3
Astrometric properties			
R.A.	(J2000.0)	23:12:14.10	Gaia DR3
Dec	(J2000.0)	-44:52:34.77	Gaia DR3
Parallax	(mas)	4.54 ± 0.03	Gaia DR3
Distance	(pc)	222.85 ± 3.69	Gaia DR3
$\mu_{R.A.}$	(mas yr^{-1})	35.86 ± 0.01	Gaia DR3
μ_{Dec}	(mas yr^{-1})	-37.62 ± 0.02	Gaia DR3
Photometric properties			
TESS	(mag)	11.527 ± 0.006	TICv8
B	(mag)	13.10 ± 0.03	TICv8
V	(mag)	12.35 ± 0.05	TICv8
G	(mag)	12.0545 ± 0.0002	Gaia DR3
J	(mag)	10.78 ± 0.02	2MASS
H	(mag)	10.41 ± 0.02	2MASS
K	(mag)	10.32 ± 0.02	2MASS

Sources: TICv8 (Stassun et al. 2019), 2MASS (Skrutskie et al. 2006), Gaia Data Release 3 (Gaia Collaboration et al. 2022).

line opportunities for further follow up of the system. Section 6 sets out our conclusions.
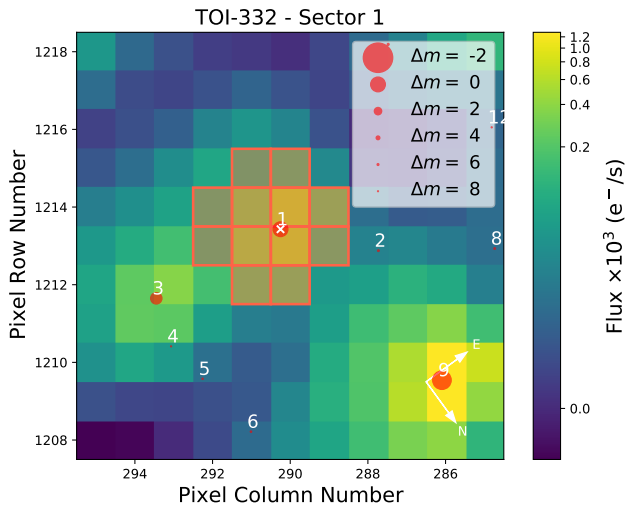
Figure 2. The Target Pixel File (TPF) for TOI-332 (marked as a white cross) from *TESS* S1. Other *Gaia* DR3 sources within a limit of 8 *Gaia* magnitudes difference from TOI-332 are marked as red circles, and are numbered in distance order from TOI-332. The aperture mask is outlined and shaded in red. This figure was created with `tpfplotter` (Aller et al. 2020).

2 OBSERVATIONS

In this section, we describe the instrumentation and observations used for the detection and characterisation of the TOI-332 system.

2.1 Photometry

2.1.1 TESS

The TOI-332 system (TIC 139285832, see Table 1) was observed in *TESS* Sectors 1 (25 July - 22 Aug 2018, hereafter S1) and 2 (22 August - 20 September 2018, hereafter S2) with a 30 min cadence in the full-frame images (FFIs). TOI-332.01 (now TOI-332 b) was detected in the FFIs by the MIT Quick-Look Pipeline (QLP, Huang et al. 2020) as part of the early *TESS* Data Alerts, and alerted on 20 December 2018 (Guerrero et al. 2021). It was then re-observed in Sector 28 (30 July - 26 August 2020, hereafter S28) on Camera 2 with a 2 min cadence. The Data Validation report (Twicken et al. 2018; Li et al. 2019) difference image centroid offsets determined from the S28 pixel data locate the transit source within 2.56 ± 2.76 arcsec of TOI-332, and exclude all other TICv8 objects as possible sources of the transit signal. The detection gave a period of 0.77685 ± 0.0003 d, a transit duration of 1.43 ± 0.442 h, and a depth of 830 ± 8 ppm. The data products, including calibrated full-frame images and light curves, are available on the Mikulski Archive for Space Telescopes (MAST; https://archive.stsci.edu/missions-and-data/transiting-exoplanet-survey-satellite-tess), and were produced by the *TESS* Science Processing Operations Center (SPOC, Jenkins et al. 2016; Caldwell et al. 2020) at NASA Ames Research Center.

We downloaded the publicly available photometry provided by the SPOC pipeline, and used the Presearch Data Conditioning Simple Aperture Photometry (PDCSAP), from which common trends and artefacts have been removed by the SPOC Presearch Data Conditioning (PDC) algorithm (Twicken et al. 2010; Smith et al. 2012; Stumpe et al. 2012, 2014). The median-normalised PDCSAP flux, after removal of data points flagged as being affected by excess noise,

is shown in Fig. 3. No further detrending of the light curves was deemed necessary as they are relatively flat across the whole time series, showing little stellar activity. We also recover no periodicity from either the PDCSAP or SAP (Simple Aperture Photometry, where no trends and artifacts have been removed) flux that may be indicative of a stellar rotation period. The phase folded transits and best fit model are also shown in Fig. 3.

2.1.2 LCOGT

The *TESS* pixel scale is ~ 21 arcsec per pixel and photometric apertures typically extend out to roughly 1 arcmin, generally causing multiple stars to blend in the *TESS* aperture (the aperture for the *TESS* S1 data for TOI-332 is shown in Fig. 2). To attempt to determine the true source of the TOI-332 detection in the *TESS* data and refine its ephemeris and transit shape, we conducted ground-based photometric follow-up observations of the field around TOI-332 as part of the *TESS* Follow-up Observing Program[1] Sub Group 1 (TFOP; Collins 2019).

We observed six full predicted transit windows of TOI-332.01 using the Las Cumbres Observatory Global Telescope (LCOGT; Brown et al. 2013) 1.0 m network nodes. The details of each observation are provided in the caption of Fig. A1. We used the TESS Transit Finder, which is a customized version of the Tapir software package (Jensen 2013), to schedule our transit observations. The 1 m telescopes are equipped with 4096 × 4096 SINISTRO cameras having an image scale of 0.389 arcsec per pixel, resulting in a 26 arcsec × 26 arcsec field of view. The images were calibrated by the standard LCOGT BANZAI pipeline (McCully et al. 2018). Differential photometric data were extracted using AstroImageJ (Collins et al. 2017). As shown in Fig. A1, we detected transit-like signals in all six TOI-332 follow-up light curves using photometric apertures with radii in the range of 3.1 arcsec to 7.8 arcsec, which exclude flux from the nearest neighbour of TOI-332 in the *Gaia* DR3 and TICv8 catalogs (which is 51 arcsec northeast, and is the target numbered 2 in Fig. 2). We therefore confirm that the TOI-332.01 signal in the *TESS* data occurs on-target relative to all known *Gaia* DR3 and TICv8 stars.

2.1.3 PEST

We observed TOI-332 in the V band from the Perth Exoplanet Survey Telescope (PEST) near Perth, Australia. At the time, the 0.3 m telescope was equipped with a 1530 × 1020 SBIG ST-8XME camera with an image scale of 1.2 arcsec per pixel resulting in a 31 arcsec × 21 arcsec field of view. A custom pipeline based on C-Munipack was used to calibrate the images and extract the differential photometry. Unfortunately, there is a gap during the transit egress due to cloud cover, and poor weather negatively affected the data quality; therefore, we do not include it in our joint fit model, but present the data with the model over-plotted in Fig. A2.

2.1.4 WASP

WASP-South, an array of 8 wide-field cameras, was the Southern station of the WASP transit-search project (Pollacco et al. 2006). It observed the field of TOI-332 in the years 2006, 2007, 2010 and 2011 when equipped with 200-mm, f/1.8 lenses, and then again in 2012, 2013 and 2014 when equipped with 85-mm, f/1.2 lenses. It observed

[1] https://tess.mit.edu/followup
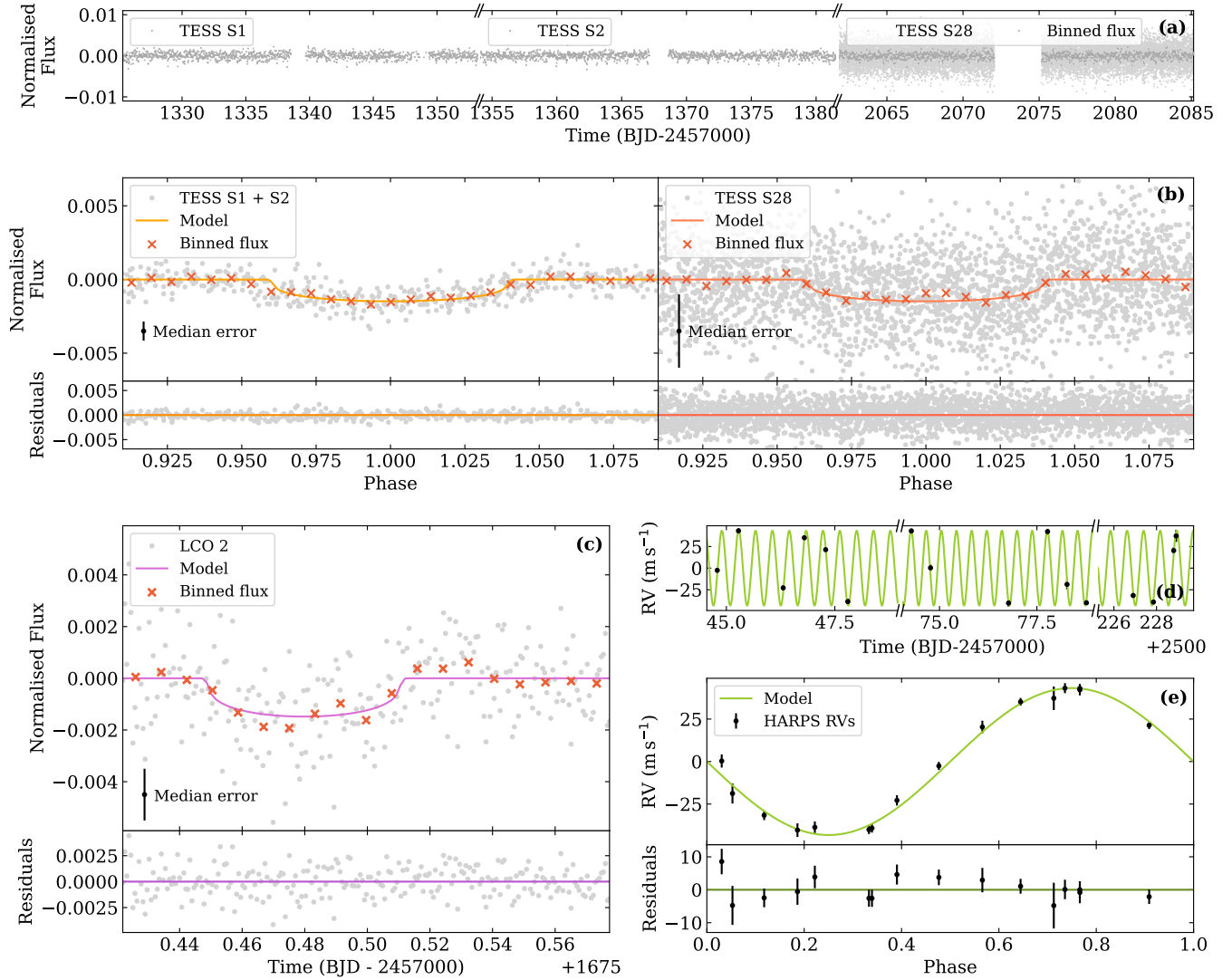
Figure 3. Joint fit model to the *TESS*, LCO, and HARPS data.

(a) *TESS* PDCSAP light curve for Sectors 1, 2 and 28 (circles), with time given as Barycentric Julian Date (BJD). Sectors 1 and 2 are 30 min cadence data, Sector 28 is 2 min cadence, hence the higher levels of noise in the latter. The Sector 28 data binned to 30 min has been overplotted in dark grey.

(b) Phase folded *TESS* 30 min cadence data (grey circles) from Sectors 1 and 2 (left), and 2 min cadence data from Sector 28 (right). Binned flux (red crosses) and the best fit model (solid line) are overplotted, and the median error on the flux is displayed (one standard deviation, black error bar, bottom left). Residuals when the model is subtracted are shown in the bottom panels.

(c) An example of the phase folded LCO data, using the second transit obtained (chronologically) by LCO (the model is fit to all of the LCO transits and the full data can be seen in Fig. A1). Symbols and model are as in **(b)**, with residuals in the bottom panel.

(d-e) The HARPS data (black circles), shown as a time series in **(d)**, and the phase folded data in **(e)**. The model is plotted as in **(b)**, with residuals in the bottom panel.

on each clear night, with a typical 10 min cadence, and accumulated 88 000 photometric data points on TOI-332.

We searched the data for any rotational modulation using the methods from Maxted et al. (2011). We find a significant periodicity in data from one year, spanning 168 nights in 2007, with an estimated false-alarm probability of 0.15 per cent. The period is 20.9 ± 1.0 d and the amplitude 3 mmag. We note that there is also a peak near 36 days, though it is not significant in itself. In 2012, a possible modulation with a similar period (18.4 ± 1.5 d) has a lower significance (8 per cent false-alarm likelihood). No significant periodicity was detected in other years. We discuss the periodicity further in Section 3.

We also note that the standard WASP transit-detection algorithm (Collier Cameron et al. 2007), when run on the same 2007 dataset, detects the transit and reports a period of 0.77663 ± 0.00012 d with an epoch of TDB 2454343.4652 ± 0.0079. The period matches the *TESS* period to 1 part in 2000 while the phase matches an extrapolated ephemeris to within 3 per cent. However, when run on the full dataset combined, the algorithm does not find the transit, though this is explainable given that red noise in other years can destroy the detection. At a depth of 0.15 per cent, the transit would be the shallowest detected in WASP data, though it is comparable to the detection of the 0.17 per cent transit of HD 219666 b (Hellier et al. 2019). We conclude that this detection is likely, but not securely,
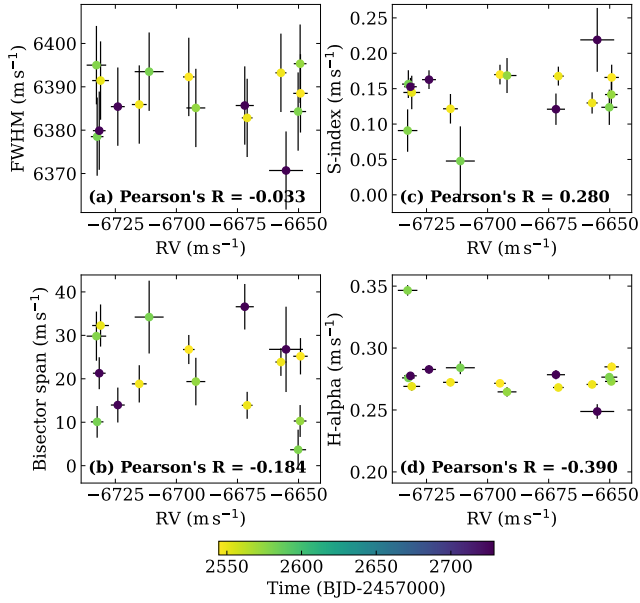
Figure 4. HARPS radial velocities plotted against stellar activity indicators:
(a), the full-width at half-maximum (FWHM) of the cross-correlation function (CCF);
(b), the bisector span of the CCF;
(c), the s-index;
and **(d)**, h-alpha.
The Pearson's R statistic, a measure of correlation strength, is given for each, and no significant correlation is seen. Colour represents the time of observation in Barycentric Julian Date (BJD). All error bars show one standard deviation.

real, and thus we report it here as the earliest detection of the transit of TOI-332 b. Since planets in short-period orbits are expected to undergo tidal decay, timings over the longest possible time span are of interest, and we discuss this further in Section 5.5.

Due to the uncertainty in the detection, we do not include the WASP data in our joint fit model, but we present the 2007 dataset with the best fit model over-plotted in Fig. A3.

2.2 Spectroscopy

2.2.1 HARPS

We made radial velocity (RV) measurements of TOI-332 with the High Accuracy Radial velocity Planet Searcher (HARPS) spectrograph mounted on the ESO 3.6 m telescope at the La Silla Observatory in Chile (Pepe et al. 2002). A total of 16 spectra were obtained between 25 November 2021 and 29 May 2022 under the HARPS-NOMADS large programme (ID 1108.C-0697, PI: Armstrong). The instrument (with resolving power $R = 115\,000$) was used in high-accuracy mode (HAM) with an exposure time of 2400 s, and 1-2 observations of the star were made per night. The data were reduced using the standard offline HARPS data reduction pipeline, and a K5 template was used in a weighted cross-correlation function (CCF) to determine the RV values (Baranne et al. 1996; Pepe et al. 2002). The line bisector (BIS) and full-width at half-maximum (FWHM) were measured using previously published methods (Boisse et al. 2011). The RV measurements can be found in Table B1, and the RV data and single-planet Keplerian best fit are shown in Fig. 3.

No correlation was detected between the RVs and the FWHM and
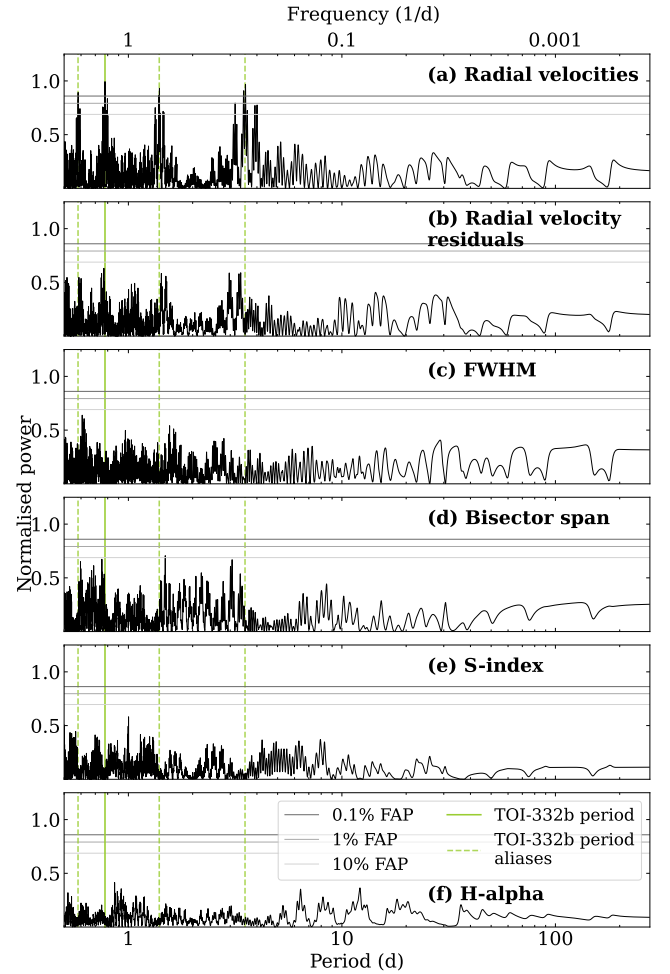
Figure 5. Periodograms for the HARPS data. The expected period of TOI-332 b is denoted by a solid vertical line, with the aliases of this period given as dashed lines. The 0.1, 1, and 10 per cent False Alarm Probabilities (FAPs) are shown as solid horizontal lines. The FAPs are calculated using the approximation from Baluev (2008). From top to bottom:
(a) the periodogram for the raw radial velocities with a peak above the 0.1 per cent FAP at the expected planetary period;
(b) the periodogram for the radial velocity residuals after the best fit model has been removed, showing no further significant peaks;
(c)-(f) the periodograms for the stellar activity indicators full-width at half-maximum (FWHM, **(c)**), bisector span **(d)**, s-index **(e)**, and h-alpha **(f)**, with no significant periodicity shown.

bisector span of the CCF, or the S and Hα activity indexes, shown in Fig. 4. After removing the contribution from TOI-332 b, we studied the RV residuals and found no evidence of further periodicity in those or in the activity indicators as shown in Fig. 5. Unfortunately, this means the RVs give no indication of a possible stellar rotation period that would corroborate that found by WASP in Section 2.1.4 or derived later in Section 3. We note that one of the Hα points, from the night of 29 December 2021, is an outlier, shown in Fig. 4. Investigating the spectrum from this night, we find a narrow emission line in the centre of the Hα line that may be indicative of a flare; however, the RV point corresponding to this night is not an outlier, nor does it have an anomalously large error, so we retain it.
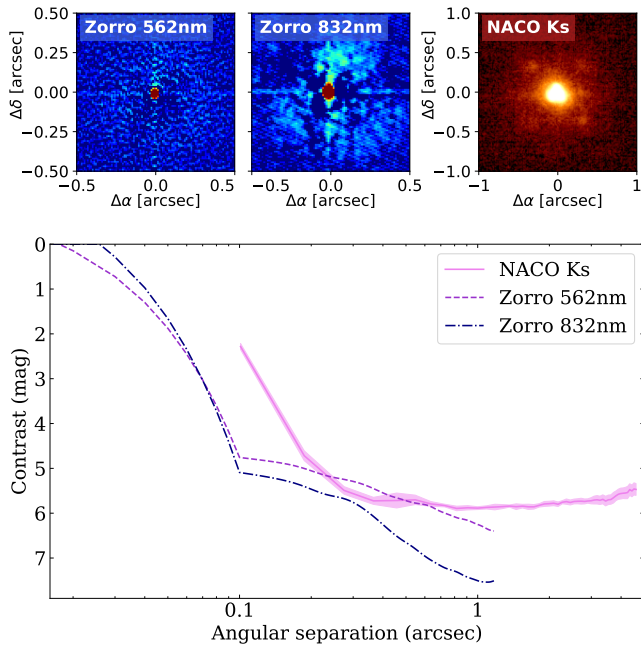
Figure 6. A compilation of reconstructed images for the sources of high-resolution imaging described in Sections 2.3.1 and 2.3.2 (top), with their corresponding 5σ contrast curves (bottom). Zorro observes simultaneously in the 562 and 832 nm bands; NACO observes in the near-IR with a Ks filter (labelled). No additional companions are detected.

2.3 High resolution imaging

2.3.1 Gemini Zorro

High-angular resolution images of TOI-332 were obtained on 10 October 2019 using the Zorro[2] speckle instrument on the Gemini-South telescope (Scott et al. 2021). Zorro observes simultaneously in two bands (832 ± 40 nm and 562 ± 54 nm), obtaining diffraction limited images with inner working angles of 0.026 and 0.017 arcsec respectively. The TOI-332 data set consisted of 5 sets of 1000×0.06 s images, which were combined using Fourier analysis techniques, examined for stellar companions, and used to produce reconstructed speckle images (see Howell et al. 2011). The speckle imaging reveals TOI-332 to be a single star with no companions detected within 1.2 arcsec down to contrast limits of ∼ 5 − 7 mag, shown in Fig. 6. At the distance of TOI-332 (220 pc), these angular limits correspond to spatial limits of 4 − 264 au.

2.3.2 VLT NaCo

We collected high-resolution adaptive optics imaging of TOI-332 with VLT/NaCo on 19 June 2019. These near-IR images complement the visible-band speckle data and provide greater sensitivity to late-type bound companions. We collected a sequence of nine images in the Ks filter, each with an integration time of 11 s; the telescope was dithered between each exposure and a sky background frame was created by median combining the science frames. We removed bad pixels, flat fielded, subtracted the sky background, and aligned the images on the stellar position before co-adding the sequence. We

calculated the sensitivity of these images by injecting fake companions at several position angles and separations, and measuring the significance to which they could be recovered.

The AO image and the sensitivity limits are presented in Fig. 6. Some extended PSF structure is seen in the image, but the star is unresolved and no companions are identified. The data reveal that TOI-332 is a single star down to 5.5 mag of contrast, beyond 365 mas from the star, and exclude bright companions beyond 100 mas.

3 SPECTROSCOPIC ANALYSIS AND CHEMICAL ABUNDANCES

Here we perform several different methods to measure and derive a range of stellar parameters for TOI-332.

We first used ARES+MOOG to derive spectroscopic stellar parameters (T_{eff}, log g, microturbulence v_{tur}, and [Fe/H]) following the same methodology as described in Santos et al. (2013); Sousa (2014); Sousa et al. (2021). The latest version of ARES [3] (Sousa et al. 2007, 2015) was used to consistently measure the equivalent widths (EW) of selected iron lines in the combined spectrum of TOI-332. For this, we used the iron line list presented in Sousa et al. (2008). The best spectroscopic parameters are found by converging into ionisation and excitation equilibrium. This process makes use of a grid of Kurucz model atmospheres (Kurucz 1993) and the radiative transfer code MOOG (Sneden 1973). We also derived a trigonometric surface gravity using *Gaia* DR3 data following the same procedure as described in Sousa et al. (2021). We find values of: T_{eff} = 5251 ± 71 K; log g = 4.46 ± 0.04 c g s; v_{tur} = 0.815 ± 0.069 km s^{-1}; and [Fe/H] = 0.256 ± 0.048 dex.

To estimate the stellar mass and radius we used the calibrations in Torres et al. (2010); because the mass is between 0.7 and 1.3 $M_\odot$ we used the correction in Santos et al. (2013). This gives $R_\star$ = 0.87 ± 0.03 R$_\odot$ and $M_\star$ = 0.88 ± 0.02 M$_\odot$.

Stellar abundances of the elements were then derived using the classical curve-of-growth analysis method assuming local thermodynamic equilibrium. The same codes and models were used for the abundance determinations. For the derivation of chemical abundances of refractory elements we closely followed the methods described in (e.g. Adibekyan et al. 2012, 2015; Delgado Mena et al. 2017). Abundances of the volatile elements, C and O, were derived following the method of Delgado Mena et al. (2021); Bertran de Lis et al. (2015). Since the two spectral lines of oxygen are usually weak and the 6300.3Å line can be contaminated by tellurics or an oxygen airglow, the EWs of these lines were manually measured with the task `splot` in IRAF. All the [X/H] ratios are obtained by doing a differential analysis with respect to a high S/N solar (Vesta) spectrum from HARPS. The abundances of these elements are presented in Table C1.

Under the assumption that stellar composition serves as a reliable indicator of the disc composition during the planet formation phase, we can determine the mass fraction of the planet building blocks. Following the methodology outlined in Santos et al. (2015, 2017), which uses a simple stoichiometric model and chemical abundances of Fe, Mg, and Si, we computed that the anticipated iron-to-silicates mass fraction is 33.5 ± 3.1 per cent.

To estimate the activity level of TOI-332, we used the HARPS

---

[2] https://www.gemini.edu/sciops/instruments/alopeke-zorro/

[3] The latest version, ARES v2, can be downloaded at https://github.com/sousasag/ARES

spectra to calculate the log R'_{HK} activity index. We co-added all spectra and used ACTIN2[4] (Gomes da Silva et al. 2018, 2021) to extract the S_{CaII} index. This index was calibrated to the Mt. Wilson scale using the calibration in Gomes da Silva et al. (2021) and converted to log R'_{HK} via Noyes et al. (1984), giving log $R'_{HK} = -4.831 \pm 0.003$. This can then be used to derive a rotation period (P_{rot}) and age of the star (τ) via the relations in Mamajek & Hillenbrand (2008), giving a rotation period of 35.6 ± 4.6 d and an age of 5.0 ± 2.3 Gyr. This rotation period is approximately twice those obtained by WASP in Section 2.1.4, and so the WASP detection could be the first harmonic rather than the true rotational period.

Moreover, we used the chemical abundances of some elements to derive an alternative value for the age through the so-called chemical clocks (i.e. certain chemical abundance ratios which have a strong correlation for age). We applied the 3D formulas described in Table 10 of Delgado Mena et al. (2019), which also consider the variation in age produced by the effective temperature and iron abundance. The chemical clocks [Y/Mg], [Y/Zn], [Y/Ti], [Y/Si], [Y/Al], [Sr/Ti], [Sr/Mg] and [Sr/Si] were used from which we obtain a weighted average age of 6.3 ± 1.8 Gyr. This age is in agreement (within errors) with the age obtained from the stellar activity and rotation.

As an independent determination of the basic stellar parameters, we performed an analysis of the broadband spectral energy distribution (SED) of the star together with the *Gaia* EDR3 parallax (with no systematic offset applied; see, e.g., Stassun & Torres 2021), in order to determine an empirical measurement of the stellar radius, following the procedures described in Stassun & Torres (2016); Stassun et al. (2017, 2018). We pulled the JHK_S magnitudes from *2MASS*, the W1–W3 magnitudes from *WISE*, the $G_{BP}G_{RP}$ magnitudes from *Gaia*, and the NUV magnitude from *GALEX*. Together, the available photometry spans the full stellar SED over the wavelength range 0.2–10 μm (see Fig. C1).

We performed a fit using Kurucz stellar atmosphere models, with the effective temperature (T_{eff}), surface gravity (log g), and metallicity ([Fe/H]) adopted from the spectroscopic analysis above. The remaining free parameter is the extinction A_V, which we limited to the maximum line-of-sight value from the Galactic dust maps of Schlegel et al. (1998). The resulting fit (Fig. C1) has a reduced χ^2 of 1.3, excluding the *GALEX* NUV flux which indicates a moderate level of activity (see below), and a best fit $A_V = 0.02 \pm 0.02$. Integrating the (unreddened) model SED gives the bolometric flux at Earth, $F_{bol} = 3.851 \pm 0.045 \times 10^{-10}$ erg s^{-1} cm^{-2}. Taking the F_{bol} and T_{eff} together with the *Gaia* parallax gives the stellar radius, $R_\star = 0.923 \pm 0.016$ R$_\odot$. In addition, we can estimate the stellar mass from the empirical relations of Torres et al. (2010), giving $M_\star = 0.96 \pm 0.06$ M$_\odot$. These broadly agree with the previous values.

Finally, to obtain another independent check on the fundamental stellar parameters, and following Fridlund et al. (2020) and references therein, we analysed our spectrum with version 5.22 of the spectral analysis package SME (Spectroscopy Made Easy; Valenti & Piskunov 1996; Piskunov & Valenti 2017). This IDL based software is used to fit the observations to synthetic stellar spectra calculated with a given set of input parameters and a suitable atmospheric grid. Here, we used the Atlas12 (Kurucz 2013) grids, together with atomic and molecular line data from VALD (Ryabchikova & Pakhomov 2015) to calculate the synthetic spectra. For T_{eff}, we modelled the line wings of the hydrogen alpha line, and derived the surface gravity, log g, from the calcium triplet λ6102, 6122, and 6162, and the λ6439 line.

---

[4] Available at https://github.com/gomesdasilva/ACTIN2.

For an independent check, we also modelled the Na I doublet at 5888/89 Å. We find $T_{eff} = 5185 \pm 100$ K and log $g = 4.4 \pm 0.1$, both in agreement with the values determined using ARES+MOOG.

We then fitted a large number of iron lines to obtain the abundances [Fe/H] = 0.4 ± 0.1 dex; [Ca/H] = 0.47 ± 0.1 dex; and [Na/H] = 0.47 ± 0.1 dex.

Following again schemes described in Fridlund et al. (2020) and keeping the macroturbulent v_{mac} and microturbulent v_{mic} velocities fixed at the empirical values found in the literature (Bruntt et al. 2010; Doyle et al. 2014), we find $v \sin i_\star = 1.5 \pm 1.2$ km s^{-1}. We can use the rotational period of 35.6 d derived earlier to estimate an equatorial velocity of ≈ 1.24 km s^{-1} (assuming spin-orbit alignment) which is in agreement with this, supporting the hypothesis of the WASP period being half the true period. We therefore take forward the 35.6 d stellar rotation period into our later analysis.

There are uncertainties on the values for $R_\star$ and $M_\star$ due to the methods used to derive them: for example, in the calculation of the synthetic models used to fit the observed spectra, and in the Torres et al. (2010) calibration used. Errors on the primary derived stellar parameters (T_{eff}, log g, [Fe/H]) are taken into account when applying the Torres et al. (2010) calibration, as explained in Santos et al. (2013).

We have used multiple methods to derive stellar parameters to account for unknown systematic effects. Our results from each method are consistent, implying that our stated errors are reasonable and the effect of unknown systematics is small. We note that any systematic errors remaining will propagate into the planetary parameters.

4 THE JOINT FIT

Using the `exoplanet` package (Foreman-Mackey et al. 2020), we fit the photometry from *TESS* and LCOGT simultaneously with the RVs from HARPS. `exoplanet` utilises the light curve modelling package `Starry` (Luger et al. 2019), `PyMC3` (Salvatier et al. 2016), and `celerite` (Foreman-Mackey et al. 2017). For consistency, all timestamps were converted to the same time system, that used by *TESS*, i.e. BJD - 2457000 (BJD-TDB). All prior distributions set on the parameters fit in this model are given in Table D1.

The photometric flux is normalised by dividing the full individual light curves by the median of their out-of-transit points and subtracting unity to produce a lightcurve with out-of-transit flux of zero. No further detrending is deemed to be necessary for either the LCOGT or *TESS* data, and so none is included in the joint fit.

To model the planetary transits, we use a limb-darkened transit model utilising the quadratic limb-darkening parameterisation in Kipping (2013) and a Keplerian orbit model. We put Gaussian priors informed by the ARES+MOOG values on the stellar radius $R_\star$ and the stellar mass $M_\star$.

The Keplerian orbit model is parameterised for the planet in terms of the orbital period P, the time of a reference midtransit t_c, the eccentricity e, and the argument of periastron ω. In an earlier iteration of this model, we found the eccentricity of TOI-332 b to be consistent with 0 (with the 95 per cent confidence interval for the eccentricity being 0 to 0.15), and so fix e and ω to 0 in the final model presented here. A close-to-zero eccentricity is also expected given the very short orbital period. These parameters are then input into light curve models created with `Starry`, alongside further parameters which are planetary radii R_p, the time series of the data t, and the exposure time t_{exp} of the instrument.

Individual light curve models are created for the LCOGT data, the combined *TESS* S1 and S2 data, and the *TESS* S28 data (S28 is kept

separate to S1 and S2 due to differing cadence and exposure time of the S1 and S2 data compared to the S28 data). We use values from the *TESS* SPOC pipeline (Li et al. 2019) to estimate the placement of wide, uninformative uniform priors for the epoch, period, and radius of TOI-332 b. For each lightcurve, we put a Gaussian prior on the offset with a mean of zero and standard deviation of one.

To fit the HARPS RVs, we use DACE[5] with a simple Keplerian model to estimate prior values for the systematic RV offset and the semi-amplitude of the RV signal K. We set wide, uninformative uniform priors on K and the offset. We also incorporate a separate jitter term with a wide Gaussian prior, the mean of which is the log of the minimum error on the HARPS data. This term encapsulates any uncharacterised signal or noise that is perceived as white noise in the RV data, for example instrumental effects and short-scale stellar activity. As the RV data does not show any significant stellar activity by visual inspection and in the stellar activity indicators (see Figs. 4 and 5), and does not exhibit any long-term trends, we do not perform any further detrending to it. This completes the joint fit model.

We use `exoplanet` to maximise the log probability of the model. The fit values that this optimisation obtains are then used as the starting point of the `PyMC3` sampler, which draws samples from the posterior using a variant of Hamiltonian Monte Carlo, the No-U-Turn Sampler (NUTS). From examination of the chains from earlier test runs of the model, we use 5 chains of 50000 steps, 1000 steps of which are discarded as burn-in. To test for non-convergence, we calculate the rank-normalised split-$\hat{R}$ statistic (Vehtari et al. 2021) for each parameter. $\hat{R} \approx 1.0$ for all parameters, implying convergence. We present our best fit parameters for the TOI-332 system from this joint fit in Table 2.

5 RESULTS AND DISCUSSION

The results of our joint fit model show that, with an orbital period of 0.777038 ± 0.000001 d, TOI-332 b is an "Ultra-Short Period" (USP) planet, defined as a planet with $P_{\rm orb} < 1$ d (Winn et al. 2018). The host star, TOI-332, is a K0 dwarf with a mass of $0.88 \pm 0.02\,M_\odot$ and a radius of $0.87^{+0.03}_{-0.02}\,R_\odot$. Assuming an albedo of zero, the proximity of the planet to the star gives the planet an equilibrium temperature of 1871^{+30}_{-26} K; it is highly irradiated, receiving approximately 2400 times the instellation of the Earth per unit area.

TOI-332 b has a mass of $57.2 \pm 1.6\,M_\oplus$, more than half the mass of Saturn, yet a radius of $3.20^{+0.16}_{-0.11}\,R_\oplus$, smaller than that of Neptune. With a density of $9.6^{+1.1}_{-1.3}$ g cm^{-3}, it is one of the densest planets of those with the size of Neptune or greater found thus far (Fig. 7). These parameters place TOI-332 b deep in the Neptunian desert (Fig. 1).

Taking all of this into account, TOI-332 b is a very interesting addition to our current Neptunian desert discoveries and a case study to test planet formation theory.

5.1 Interior structure

As seen in Fig. 7, TOI-332 b occupies a unique and unpopulated spot in the mass-radius (M-R) diagram. Its mass and radius suggest a composition that is dominated by refractory materials, potentially more similar to that of terrestrial planets.

To put limits on the possible composition of TOI-332 b, we use a layered interior model similar to those used in Dorn et al. (2017) and Armstrong et al. (2020). This model consists of up to four layers

including an iron core, a silicate mantle, a water layer, and a H-He atmosphere. For these layers, we solve the standard structure equations to estimate the possible ranges of H-He mass fractions. We note, however, that for such high mass planets, layers might not be as distinct as assumed here (e.g., Helled & Stevenson 2017; Bodenheimer et al. 2018). Overall, the planet is found to consist of 30 per cent iron core, 43 per cent rock mantle, 27 per cent water, and a negligible H-He envelope.

To constrain the H-He mass, we investigate the extreme situation of a planet without water and compare it with a planet where the water abundance is allowed to vary freely. For these cases, we construct structure models that reproduce the measured mass and radius of TOI-332 b. Moreover, we assume host star elemental abundances.

We find that even if TOI-332 b had no water, the H-He mass fraction would be only $1.8^{+0.6}_{-0.5}$ %. In the water-containing model, the H-He mass fraction is $\log(M_{\rm atm}/M_{\rm p}) = -6.7 \pm 3.2$, well below 0.1 per cent. We can therefore conclude that, unless the planet is devoid of water, the atmospheric mass of TOI-332 b is very small.

Typically, planets with comparable masses to TOI-332 b are expected to be H-He dominant in composition, and terrestrial planets are not expected to reach several tens of Earth masses. Planetary embryos are expected to accrete only a few to ~20 Earth masses of heavy elements before the onset of rapid gas accretion (e.g., Pollack et al. 1996; Lambrechts et al. 2014; Piso et al. 2015), resulting in a large envelope. However, with such a large core mass and little envelope, the existence of TOI-332 b requires further explanation, perhaps having lost an initial envelope, or having managed to avoid core-accretion. We explore several scenarios below.

5.2 Co-orbital bodies

To try and explain the apparently excessive core mass of TOI-332 b, we first tested an alternative co-orbital configuration of two planets which may mimic the appearance of a single, more massive planet, and compare its evidence against the current one-planet scenario.

Co-orbital exoplanets (pairs of planets trapped in 1:1 resonances) are dynamically stable under very soft conditions (Laughlin & Chambers 2002), and several formation mechanisms have already been proposed for these configurations (see e.g., Beaugé et al. 2007; Namouni & Morais 2017; Leleu et al. 2019). However, no co-orbital exoplanets have yet been found despite several efforts (e.g., Janson 2013; Hippke & Angerhausen 2015; Ford & Holman 2007; Madhusudhan & Winn 2009; Lillo-Box et al. 2018a,b), although different candidates have already been proposed (e.g., Lillo-Box et al. 2014; Boyajian et al. 2016; Lillo-Box et al. 2020).

In the particular case of TOI-332 b, we explore the scenario where this planet is actually a pair of planets in 1:1 resonance where the lighter planet transits the host star while the more massive component does not. Assuming a low eccentricity scenario, we can approximate the sum of two Keplerians with the same periodicity as a single Keplerian. We might attribute the mass of the more massive (non-transiting) component to the only component that we see transiting the host star. This will imprint specific features in the radial velocity data that are testable through available techniques. In particular, in order to test this scenario, we apply the technique described in Leleu et al. (2017) (a generalisation of the technique proposed by Ford & Gaudi (2006)), which combines the transit and radial velocity information to infer time lags between the time of transit and the radial velocity phase. This technique is based on the modelling of the radial velocity data assuming the time of conjunction and period derived from the transit modelling. In this case, we assume the value $t_c = 2459062.444852864292$ and and $P = 0.77703814$ days, obtained

---

Table 2. Stellar parameters of TOI-332, and transit, orbital, and physical parameters of TOI-332 b (further parameters from the joint fit model can be found in Table D1).

Parameter	(unit)	Value	Source
Host star			
Distance to Earth	(pc)	222.85 ± 3.69	Gaia DR3
Effective temperature T_{eff}	(K)	5251 ± 71	ARES+MOOG
Spectral type	-	K0V	Pecaut & Mamajek (2013)
Surface gravity $\log g$	(c g s)	4.46 ± 0.04	ARES+MOOG
Metallicity [Fe/H]	(dex)	0.256 ± 0.048	ARES+MOOG
Stellar radius $R_\star$	$(R_\odot)$	$0.87^{+0.03}_{-0.02}$	Joint fit
Stellar mass $M_\star$	$(M_\odot)$	0.88 ± 0.02	Joint fit
Rotational velocity $v \sin i_\star$	(km s^{-1})	$< 1.5 \pm 1.2$	SME
Chromospheric activity index $\log R'_{\mathrm{HK}}$	-	-4.831 ± 0.003	ACTIN2
Rotation period P_{rot}	(days)	35.6 ± 4.6	$\log R'_{\mathrm{HK}}$ + Mamajek & Hillenbrand (2008)
Age τ	(Gyr)	5.0 ± 2.3	$\log R'_{\mathrm{HK}}$ + Mamajek & Hillenbrand (2008)
Planet			
Period P	(days)	0.777038 ± 0.000001	Joint fit
Full transit duration T_{dur}	(hours)	1.52 ± 0.03	Joint fit (derived)
Reference time of midtransit t_c	(BJD-2457000)	$2062.4447^{+0.0006}_{-0.0005}$	Joint fit
Radius R_P	$(R_\oplus)$	$3.20^{+0.16}_{-0.11}$	Joint fit
Planet-to-star radius ratio $R_P/R_\star$	-	0.0341 ± 0.0009	Joint fit (derived)
Impact parameter b	-	$0.25^{+0.13}_{-0.15}$	Joint fit
Inclination i	(°)	$86.4^{+2.3}_{-2.0}$	Joint fit
Eccentricity e	-	0 (fixed)	Joint fit
The argument of periastron ω	(°)	0 (fixed)	Joint fit
Radial velocity semi-amplitude K	(ms^{-1})	43 ± 1	Joint fit
Mass M_P	$(M_\oplus)$	57.2 ± 1.6	Joint fit (derived)
Bulk density ρ	(g cm^{-3})	$9.6^{+1.1}_{-1.3}$	Joint fit (derived)
Semi-major axis a	(AU)	0.0159 ± 0.0001	Joint fit (derived)
System scale $a/R_\star$	-	$3.94^{+0.11}_{-0.12}$	Joint fit (derived)
Equilibrium temperature* T_{eq}	(K)	1871^{+30}_{-25}	Joint fit (derived)

*Equilibrium temperature is calculated assuming an albedo of zero.
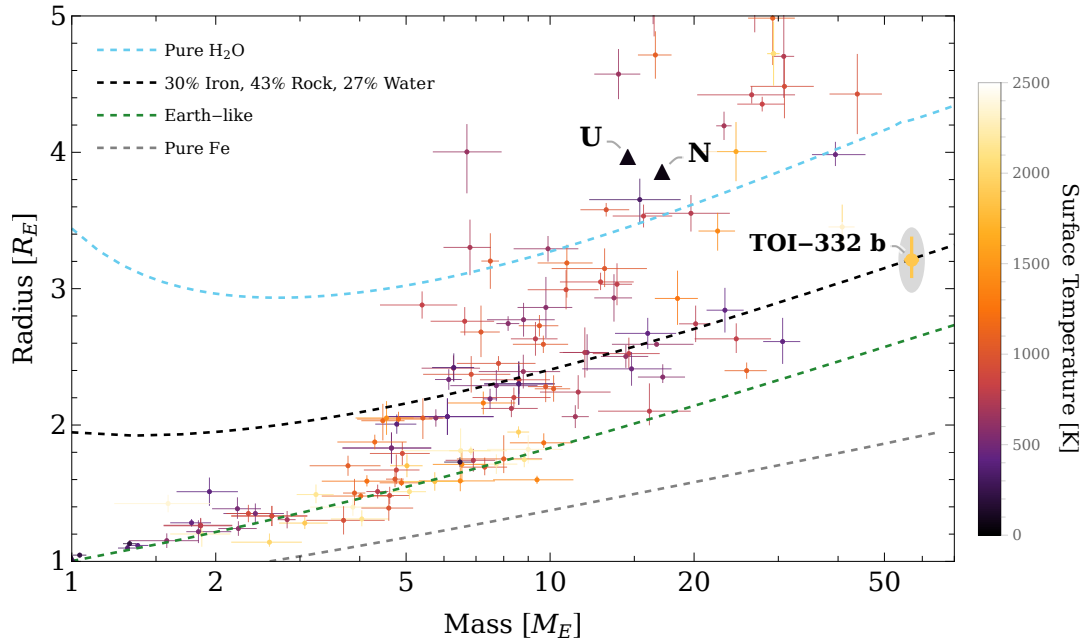
Figure 7. Mass-radius diagram of the exoplanets in the Otegi catalog (Otegi et al. 2020). The color of the planets indicates their equilibrium temperature. The dashed blue, green, and gray line show the mass-radius relation for a pure water, an Earth-like, and a pure iron composition at TOI-332 b's equilibrium temperature (1869.4 K), respectively. Uranus and Neptune are shown as black triangles.

only by modelling the photometry from *TESS* and LCOGT. We apply Equation 18 in Leleu et al. (2017), which includes the RV semi-amplitude K, the orbital configuration parameters (c and d), and the additional parameter α, a measure of the mass imbalance between the Lagrangian regions L_4 and L_5.

Here we test four different models: two assuming only one planet in the orbit (one assuming a circular orbit, "1p(c)", the other including the possibility of a slightly eccentric orbit, "1p"), and two including the co-orbital scenario (again, one assuming a circular orbit, "1p(c)T", and the other leaving the eccentricity as a free parameter, "1pT"). We use the implementation of Goodman & Weare (2010)'s affine invariant Markov chain Monte Carlo (MCMC) ensemble sampler emcee (Foreman-Mackey et al. 2013) to sample the posterior probability distribution of each of these parameters. The MCMC chains are subsequently used to estimate the Bayesian evidence ($\ln \mathcal{Z}_i$) of the models using the perrakis implementation (Díaz et al. 2016).

The results of our analysis show the model with just one planet in circular orbit as the most favourable model based on the current dataset ($\Delta \ln \mathcal{Z} > +7$ against the other more complex models). Consequently we can conclude that the current dataset does not support the presence of an additional co-orbital planet, hence confirming that all the mass at this periodicity is accumulated into the transiting body. For the simpler co-orbital model with circular orbit, we obtain $\alpha = -0.031^{+0.032}_{-0.031}$, hence compatible with zero (i.e., no mass imbalance between L4 and L5 and so potentially no co-orbitals) at the 1σ level.

5.3 Evolution under XUV-driven escape

We then test whether a TOI-332 b-like planet could be reproduced by stripping an initial accreted envelope through X-ray and extreme-ultraviolet (EUV; together, XUV) driven escape.

We performed simulations on the evaporation history of TOI-332 b by taking into account the range of possible XUV emission histories of the star motivated by its stellar parameters. We fitted the star's inferred spin period of 35.6 ± 4.6 days with the rotational evolution models of Johnstone et al. (2021) and estimated a gyrochronological age of $5.3^{+1.5}_{-1.4}$ Gyr.

By field age, the initial spread in stellar rotation periods have largely converged to a single track, leaving their histories degenerate, i.e., we cannot tell which history TOI-332 followed. We thus considered three spin histories in order to sample the diversity of possible X-ray activity pasts experienced by the planet: the *low*, *medium*, and *high* activity scenarios, which represent the model's 5th, 50th, and 95th percentiles in the distribution of rotation periods at any given age. These rotational histories are shown in Fig. 8 (left hand panel), together with the star's current place along these tracks. The corresponding XUV luminosity tracks for these scenarios are shown in Fig. 8 (right hand panel).

We then simulated the evaporation history of TOI-332 b using the *photoevolver* code[6] (Fernández Fernández et al. 2023). For this analysis, we adopted the full hydrodynamic model of Kubyshkina et al. (2018) (and the interpolation routine of Kubyshkina & Fossati (2021)) to calculate the mass loss rates.

Taking the results of the interior structure characterisation, we assumed that the planet is currently a bare core with no gaseous envelope. We can thus estimate an upper limit on the initial envelope mass fraction assuming that it has just finished evaporating. Over this upper limit, the envelope would fail to evaporate in the lifetime of the planet, and this would be inconsistent with the planet's current structure.

We achieved this by adding a tiny amount of gas to the planet, equivalent to 0.01 per cent of its total mass (such that it is completely evaporated within one simulation time step), and evolved this tenuous atmosphere backwards in time to the age of 10 Myr. We repeated this process using each of the three XUV emission scenarios, and plot the results in Fig. 9.

We find that the possible evaporation histories for TOI-332 b based on these scenarios lead to a narrow range of upper limits on the initial envelope mass fraction, between 3 and 6 per cent. We thus find that TOI-332 b starting out as a Jupiter-sized planet is inconsistent with photoevaporation as the only mechanism for mass loss.

5.4 Other formation scenarios

It is clear that if TOI-332 b originally had a Jupiter-like envelope as we would expect for a core of this size, photoevaporation could not have been the sole mechanism responsible for the removal of most of its atmosphere. So we can theorise other scenarios that could have caused this. An initially large envelope may have been removed by high-eccentricity migration and subsequent tidal thermalisation (e.g. Ivanov & Papaloizou 2004; Vick & Lai 2018; Wu 2018; Vick et al. 2019). Alternatively, the atypical composition of TOI-332 b could be the result of a giant impact between two gas giants followed by efficient removal of the gaseous atmosphere (e.g. Liu et al. 2015; Emsenhuber et al. 2021; Ogihara et al. 2021). Finally, runaway accretion could have just been avoided entirely by, for example, gap opening in the protoplanetary disk (e.g. Crida et al. 2006; Duffell & MacFadyen 2013; Lee 2019).

However, we do not think it is currently possible to say which, if any, of these formation scenarios created TOI-332 b, though future observations may aid us in this.

5.5 Orbital decay rate

As TOI-332 b is both unusually massive and close to its host star, it may be one of the most well-placed non-gas giant planets for an orbital decay rate study.

We follow the method outlined in Jackson et al. (2023) to calculate the orbital decay rate, dP/dt. In short, we use the following equation (Goldreich & Soter 1966; Ogilvie 2014):

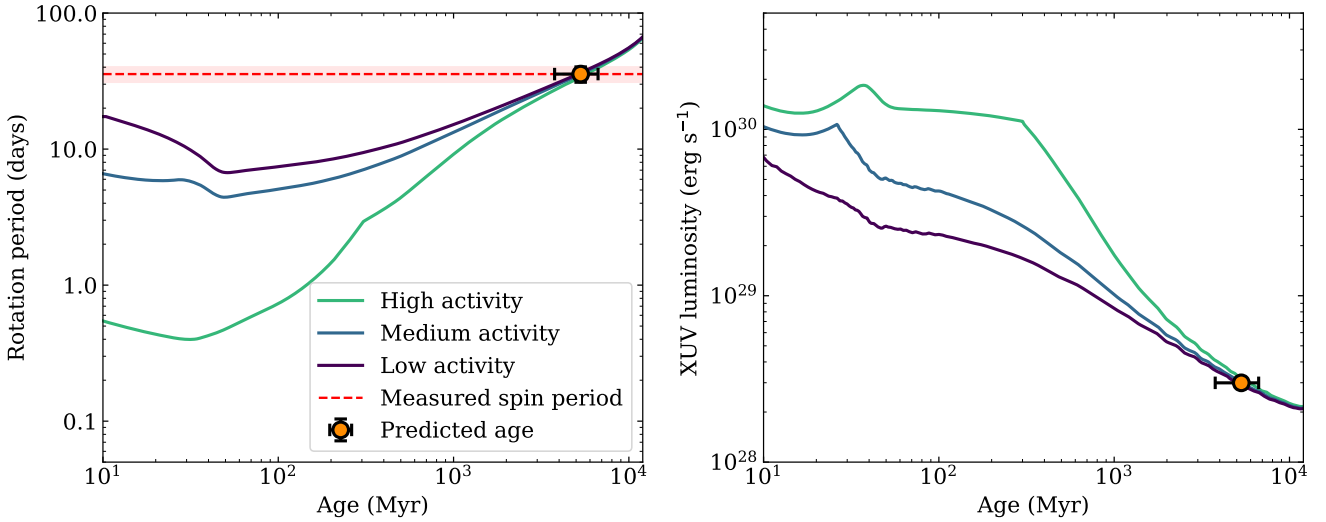$$\frac{dP}{dt} = -\frac{27\pi}{2Q'_*} \left(\frac{M_p}{M_\star}\right) \left(\frac{R_*}{a}\right)^5 \tag{1}$$

where $Q'_* = 3Q_*/2k_2$. Q_* is the tidal quality factor, Q'_* is the reduced tidal quality factor, and k_2 is the dimensionless quadrupolar Love number.

We do not consider the dynamical tide within the convective zone, only the equilibrium tide, as the orbital period of the planet is much less than twice the stellar rotation period. This allows us to calculate Q'_* as defined in Strugarek et al. (2017), which requires a value for the depth of the convective zone[7].

We find $Q'_* = 8 \times 10^6$, resulting in $dP/dt = -1.05 \times 10^{-12}$. We use the decay rate together with the period to estimate the length of time

---

[6] The evaporation evolution code is available on GitHub at https://github.com/jorgefz/photoevolver

[7] We estimate the radius and mass of the stellar core using http://www.astro.wisc.edu/~townsend/static.php?ref=ez-web.

Figure 8. Left panel: plot of rotation period against age showing rotational evolution models by Johnstone et al. (2021), with high, medium, and low activity tracks for a 0.9 M$_\odot$ star. Its measured rotation period is shown as a dashed red line, with the uncertainty as a shaded region. The age estimated with gyrochronology is plotted as an orange circle. **Right panel:** plot of XUV luminosity against age showing the corresponding XUV evolution tracks to the models on the left panel, as well as the predicted XUV luminosity based on its rotation period. The models were calculated using the methods described in Section 5.3.
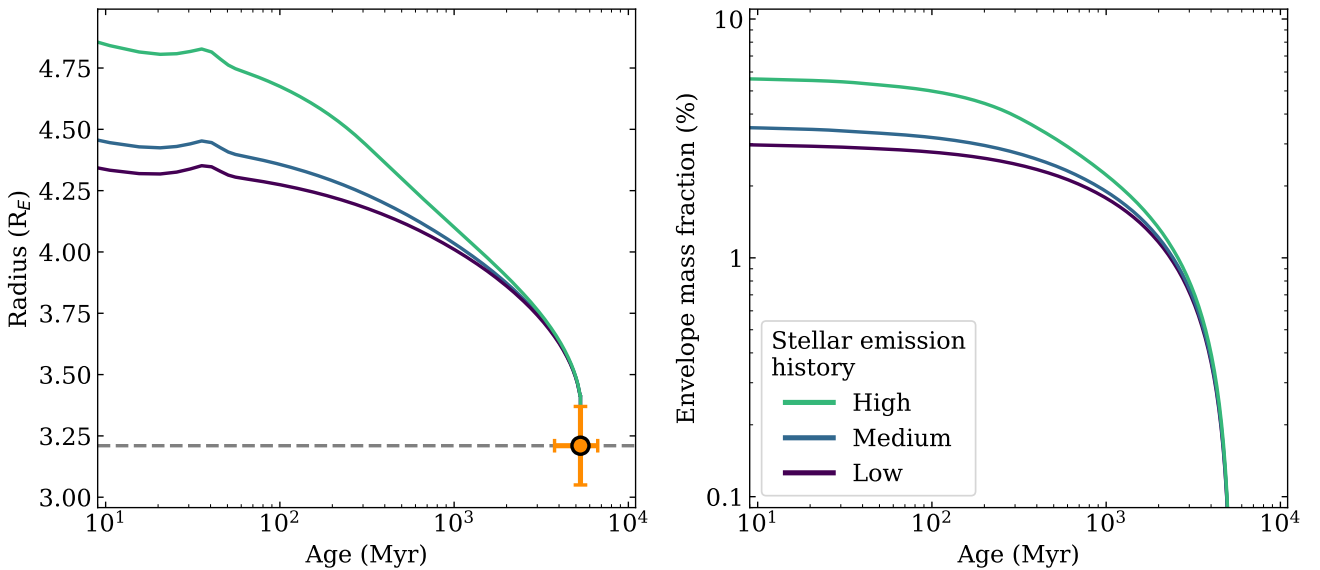
Figure 9. Left panel: plot of planet radius against age showing the evolution of the radius of TOI-332 b using the three stellar XUV emission histories described in Section 5.3. **Right panel:** plot of envelope mass fraction against age showing the evolution of the past envelope mass of TOI-332 b following the left panel.

it would take for the orbit to decay completely (i.e. reaching a period of zero) as 2.0 Gyr. We note that this is a likely upper-estimate of the decay timescale, as it assumes a constant rate of decay, ignoring any effects that may alter this (e.g. stellar wind and stellar evolution). Our method also does not take into account the structure of the planet, which some other more complex treatments of tidal effects do (e.g. Henning & Hurford 2014; Clausen & Tilgner 2015; Brasser et al. 2019), but this is beyond the scope of this paper.

We can also estimate boundaries on this decay timescale by as-

suming upper and lower limits on Q'_* of 10^5 and 10^8, resulting in timescales of 0.25 and 250 Gyr respectively. Even the shortest decay timescale of 0.25 Gyr is several magnitudes longer than the current decay timescale estimate for WASP-12 b of 3.16 ± 0.10 Myr, to date the only planet we have confidently detected an orbital decay for (Maciejewski et al. 2016; Patra et al. 2017, 2020; Yee et al. 2020; Wong et al. 2022). Thus we conclude that measuring the orbital decay of TOI-332 b is not going to be possible over a realistic span of time.

5.6 Future observation prospects

TOI-332 b is undoubtedly an unusual and unique planet, and further observations will be needed to deduce more about its formation and evolutionary history and its current composition.

The Rossiter-McLaughlin (RM) effect allows us to measure the sky-projected obliquity of a system, and is important for constraining formation scenarios: disk-migration is expected to conserve alignment between the angular momentum of a disk and planetary orbits, but misalignment could imply, for example, planet-planet/planet-star scattering, high-eccentricity migration, or tidal disruption. If TOI-332 b lacks an atmosphere due to reduced gas accretion through gap opening, it should align to the stellar spin axis, but if it is misaligned, it might imply a more violent history has removed an initial envelope - though at such a short period, there is the possibility that tides might cause realignment even if the orbit and stellar spin axis began misaligned. We can predict a RM semi-amplitude of approximately $2.1 \, \mathrm{m \, s^{-1}}$ (Triaud 2018); though this signal is small, smaller RM amplitudes have been measured (e.g. Winn et al. 2010; Bourrier & Hébrard 2014) and are obtainable with high-precision spectrographs like HARPS/HARPS-N and ESPRESSO, and methods such as the Rossiter-McLaughlin effect Revolutions (RMR) technique (Bourrier et al. 2021).

There is evidence from other USP planet discoveries that they often have companions with periods out to 50 days (Sanchis-Ojeda et al. 2014), and for a system like TOI-332 with $a/R_\star < 5$ they'd be expected to have a minimum mutual inclination of $5 - 10$ deg (Dai et al. 2018). We find no evidence of a companion in our current data, photometric or spectroscopic; further long-term monitoring of this system would be needed to discover or rule out a companion, and this may also help narrow down formation scenarios for this system.

Characterising potentially unusual atmospheres and surfaces of highly-irradiated rocky worlds is an exciting prospect. While the predicted atmospheric mass fraction of TOI-332 b is small, the high equilibrium temperature of TOI-332 b may lead to evaporation of volatiles and formation of a secondary atmosphere that could contain core materials. The composition of such an atmosphere could be determined with JWST. Additionally, JWST could be used to obtain a phase curve of TOI-332 b, which would constrain its dayside and nightside temperatures and any phase offset, its Bond albedo, and heat recirculation efficiency. With little atmosphere we would expect high temperature contrast and poor recirculation, and may be able to distinguish between different surface composition scenarios.

6 CONCLUSION

We present here the discovery and characterisation of a new planet in the TOI-332 system. We use photometry from two *TESS* sectors at 30 min cadence and one sector at 2 min cadence, plus six LCOGT transit events. There is further photometry from PEST and WASP-South, but this was not included in the final fit due to the ambiguity of the transit detections. The photometric data were modelled jointly with 16 RV data points from the HARPS spectrograph. Multiple sources of high-resolution imaging confirm that the star is single with no unresolved companions.

The planet TOI-332 b is on an ultra-short period of 0.78 days, with a radius smaller than Neptune but an anomalously large mass of more than half that of Saturn, making it one of the densest known Neptune-sized planets discovered thus far. It is located deep within the Neptunian desert, and is one of only a handful of planets that have been found there, being one of even fewer to have a precise mass determination. Using a four layer model consisting of an iron core, silicate mantle, water, and a H-He envelope, interior structure characterisation determines that it likely possesses a negligible H-He envelope.

This unusual planet tests what we currently understand about planet formation; how such a giant core exists without a gaseous envelope remains an unanswered question. We determine that photoevaporation would be insufficient on its own in removing a Jupiter-like envelope, and we instead posit high-eccentricity migration or giant impacts as possible mechanisms for stripping the initial envelope from TOI-332 b. Alternatively, a mechanism like disc-gap opening could have led it to avoid gas accretion in the first instance. Further observations are needed to potentially disentangle TOI-332 b's formation history and current characteristics.

This research has made use of the NASA Exoplanet Archive, which is operated by the California Institute of Technology, under contract with the National Aeronautics and Space Administration under the Exoplanet Exploration Program.

This research made use of exoplanet (Foreman-Mackey et al. 2020) and its dependencies (Agol et al. 2020; Kumar et al. 2019; Astropy Collaboration et al. 2013, 2018; Kipping 2013; Luger et al. 2019; Salvatier et al. 2016; Theano Development Team 2016).

This publication makes use of The Data & Analysis Center for Exoplanets (DACE), which is a facility based at the University of Geneva (CH) dedicated to extrasolar planets data visualisation, exchange and analysis. DACE is a platform of the Swiss National Centre of Competence in Research (NCCR) PlanetS, federating the Swiss expertise in Exoplanet research. The DACE platform is available at https://dace.unige.ch.

This paper made use of data collected by the TESS mission and are publicly available from the Mikulski Archive for Space Telescopes (MAST) operated by the Space Telescope Science Institute (STScI). Funding for the TESS mission is provided by NASA's Science Mission Directorate. We acknowledge the use of public TESS data from pipelines at the TESS Science Office and at the TESS Science Processing Operations Center. Resources supporting this work were provided by the NASA High-End Computing (HEC) Program through the NASA Advanced Supercomputing (NAS) Division at Ames Research Center for the production of the SPOC data products.

This research has made use of the Exoplanet Follow-up Observation Program (ExoFOP; DOI: 10.26134/ExoFOP5) website, which is operated by the California Institute of Technology, under contract with the National Aeronautics and Space Administration under the Exoplanet Exploration Program.

This work makes use of observations from the LCOGT network. Part of the LCOGT telescope time was granted by NOIRLab through the Mid-Scale Innovations Program (MSIP). MSIP is funded by NSF.

Some of the observations in this paper made use of the High-Resolution Imaging instrument Zorro and were obtained under Gemini LLP Proposal Number: GN/S-2021A-LP-105. Zorro was funded by the NASA Exoplanet Exploration Program and built at the NASA Ames Research Center by Steve B. Howell, Nic Scott, Elliott P. Horch, and Emmett Quigley. Zorro was mounted on the Gemini South telescope of the international Gemini Observatory, a program of NSF's OIR Lab, which is managed by the Association of Universities for Research in Astronomy (AURA) under a cooperative agreement with the National Science Foundation. on behalf of the Gemini partnership: the National Science Foundation (United States), National Research Council (Canada), Agencia Nacional de Investigación y Desarrollo (Chile), Ministerio de Ciencia, Tecnología e Innovación (Argentina), Ministério da Ciência, Tecnologia, Inovações e Comunicações (Brazil), and Korea Astronomy and Space Science Institute (Republic of Korea).

This work made use of tpfplotter by J. Lillo-Box (publicly available in www.github.com/jlillo/tpfplotter), which also made use of the python packages astropy, lightkurve, matplotlib and numpy.

DATA AVAILABILITY

The *TESS* data are available from the Mikulski Archive for Space Telescopes (MAST), at https://heasarc.gsfc.nasa.gov/docs/tess/data-access.html. The other photometry from LCOGT and PEST, and the high-resolution imaging data, are available for public download from the ExoFOP-TESS archive at https://exofop.ipac.caltech.edu/tess/target.php?id=139285832. The full HARPS RV data products are publicly available from the ESO archive, at http://archive.eso.org/wdb/wdb/adp/phase3_main/form. The model code underlying this article will be shared on reasonable request to the corresponding author. The MCMC chains are available from Zenodo, at https://doi.org/10.5281/zenodo.8199962.

REFERENCES

Adibekyan V. Z., Sousa S. G., Santos N. C., Delgado Mena E., González Hernández J. I., Israelian G., Mayor M., Khachatryan G., 2012, A&A, 545, A32

Adibekyan V., et al., 2015, A&A, 583, A94

Agol E., Luger R., Foreman-Mackey D., 2020, AJ, 159, 123

Aller A., Lillo-Box J., Jones D., Miranda L. F., Barceló Forteza S., 2020, A&A, 635, A128

Armstrong D. J., et al., 2020, Nature, 583, 39

Astropy Collaboration et al., 2013, A&A, 558, A33

Astropy Collaboration et al., 2018, aj, 156, 123

Baluev R. V., 2008, MNRAS, 385, 1279

Baranne A., et al., 1996, A&AS, 119, 373

Barragán O., et al., 2019, MNRAS, 490, 698

Beaugé C., Nesvorný D., 2013, ApJ, 763, 12

Beaugé C., Sándor Z., Érdi B., Süli Á., 2007, A&A, 463, 359

Bertran de Lis S., Delgado Mena E., Adibekyan V. Z., Santos N. C., Sousa S. G., 2015, A&A, 576, A89

Bodenheimer P., Stevenson D. J., Lissauer J. J., D'Angelo G., 2018, ApJ, 868, 138

Boisse I., Bouchy F., Hébrard G., Bonfils X., Santos N., Vauclair S., 2011, A&A, 528, A4

Borucki W. J., et al., 2010, Science, 327, 977

Boué G., Figueira P., Correia A. C. M., Santos N. C., 2012, A&A, 537, L3

Bourrier V., Hébrard G., 2014, A&A, 569, A65

Bourrier V., et al., 2021, A&A, 654, A152

Bourrier V., et al., 2023, A&A, 669, A63

Boyajian T. S., et al., 2016, MNRAS, 457, 3988

Brasser R., Barr A. C., Dobos V., 2019, MNRAS, 487, 34

Brown T. M., et al., 2013, PASP, 125, 1031

Bruntt H., et al., 2010, MNRAS, 405, 1907

Caldwell D. A., et al., 2020, Research Notes of the American Astronomical Society, 4, 201

Clausen N., Tilgner A., 2015, A&A, 584, A60

Collier Cameron A., et al., 2007, MNRAS, 380, 1230

Collins K., 2019, in American Astronomical Society Meeting Abstracts #233. p. 140.05

Collins K. A., Kielkopf J. F., Stassun K. G., Hessman F. V., 2017, AJ, 153, 77

Crida A., Morbidelli A., Masset F., 2006, Icarus, 181, 587

Dai F., Masuda K., Winn J. N., 2018, ApJ, 864, L38

Dawson R. I., Johnson J. A., 2018, ARA&A, 56, 175

Delgado Mena E., Tsantaki M., Adibekyan V. Z., Sousa S. G., Santos N. C., González Hernández J. I., Israelian G., 2017, A&A, 606, A94

Delgado Mena E., et al., 2019, A&A, 624, A78

Delgado Mena E., Adibekyan V., Santos N. C., Tsantaki M., González Hernández J. I., Sousa S. G., Bertrán de Lis S., 2021, A&A, 655, A99

Díaz R. F., et al., 2016, A&A, 585, A134

Dorn C., Venturini J., Khan A., Heng K., Alibert Y., Helled R., Rivoldini A., Benz W., 2017, A&A, 597, A37

Doyle A. P., Davies G. R., Smalley B., Chaplin W. J., Elsworth Y., 2014, MNRAS, 444, 3592

Duffell P. C., MacFadyen A. I., 2013, ApJ, 769, 41

Emsenhuber A., Mordasini C., Burn R., Alibert Y., Benz W., Asphaug E., 2021, A&A, 656, A70

Fernández Fernández J., Wheatley P. J., King G. W., 2023, arXiv e-prints, p. arXiv:2304.12705

Ford E. B., Gaudi B. S., 2006, ApJ, 652, L137

Ford E. B., Holman M. J., 2007, ApJ, 664, L51

Foreman-Mackey D., Hogg D. W., Lang D., Goodman J., 2013, PASP, 125, 306

Foreman-Mackey D., Agol E., Ambikasaran S., Angus R., 2017, celerite: Scalable 1D Gaussian Processes in C++, Python, and Julia (ascl:1709.008)

Foreman-Mackey D., Czekala I., Luger R., Agol E., Barentsen G., Barclay T., 2020, exoplanet-dev/exoplanet v0.2.6, doi:10.5281/zenodo.1998447, https://doi.org/10.5281/zenodo.1998447

Fridlund M., et al., 2020, MNRAS, 498, 4503

Gaia Collaboration et al., 2022, arXiv e-prints, p. arXiv:2208.00211

Goldreich P., Soter S., 1966, Icarus, 5, 375

Gomes da Silva J., Figueira P., Santos N., Faria J., 2018, The Journal of Open Source Software, 3, 667

Gomes da Silva J., et al., 2021, A&A, 646, A77

Goodman J., Weare J., 2010, Communications in Applied Mathematics and Computational Science, 5, 65

Guerrero N. M., et al., 2021, ApJS, 254, 39

Helled R., Stevenson D., 2017, ApJ, 840, L4

Helled R., Lozovsky M., Zucker S., 2016, MNRAS, 455, L96

Hellier C., Anderson D. R., Gill S., West R. G., 2019, Research Notes of the American Astronomical Society, 3, 156

Henning W. G., Hurford T., 2014, ApJ, 789, 30

Hippke M., Angerhausen D., 2015, ApJ, 811, 1

Howell S. B., Everett M. E., Sherry W., Horch E., Ciardi D. R., 2011, AJ, 142, 19

Huang C. X., et al., 2020, Research Notes of the American Astronomical Society, 4, 204

Ivanov P. B., Papaloizou J. C. B., 2004, MNRAS, 347, 437

Jackson D. G., et al., 2023, MNRAS, 518, 4845

Janson M., 2013, ApJ, 774, 156

Jenkins J. M., et al., 2016, in Chiozzi G., Guzman J. C., eds, Society of Photo-Optical Instrumentation Engineers (SPIE) Conference Series Vol. 9913, Software and Cyberinfrastructure for Astronomy IV. p. 99133E, doi:10.1117/12.2233418

Jenkins J. S., et al., 2020, Nature Astronomy, 4, 1148

Jensen E., 2013, Tapir: A web interface for transit/eclipse observability, Astrophysics Source Code Library, record ascl:1306.007 (ascl:1306.007)

Johnstone C. P., Bartel M., Güdel M., 2021, A&A, 649, A96

Kipping D. M., 2013, mnras, 435, 2152

Kubyshkina D. I., Fossati L., 2021, Research Notes of the American Astronomical Society, 5, 74

Kubyshkina D., et al., 2018, ApJ, 866, L18

Kumar R., Carroll C., Hartikainen A., Martin O. A., 2019, The Journal of Open Source Software

Kurucz R. L., 1993, SYNTHE spectrum synthesis programs and line data. Smithsonian Astrophysical Observatory

Kurucz R. L., 2013, ATLAS12: Opacity sampling model atmosphere program, Astrophysics Source Code Library, record ascl:1303.024 (ascl:1303.024)

Lambrechts M., Johansen A., Morbidelli A., 2014, A&A, 572, A35

Laughlin G., Chambers J. E., 2002, AJ, 124, 592

Lee E. J., 2019, ApJ, 878, 36

Leleu A., Robutel P., Correia A. C. M., Lillo-Box J., 2017, A&A, 599, L7

Leleu A., Coleman G. A. L., Ataiee S., 2019, A&A, 631, A6

Li J., Tenenbaum P., Twicken J. D., Burke C. J., Jenkins J. M., Quintana E. V., Rowe J. F., Seader S. E., 2019, PASP, 131, 024506

Lillo-Box J., et al., 2014, A&A, 562, A109

Lillo-Box J., Barrado D., Figueira P., Leleu A., Santos N. C., Correia A. C. M., Robutel P., Faria J. P., 2018a, A&A, 609, A96

Lillo-Box J., et al., 2018b, A&A, 618, A42

Lillo-Box J., et al., 2020, A&A, 642, A121

Liu S.-F., Agnor C. B., Lin D. N. C., Li S.-L., 2015, MNRAS, 446, 1685

Livingston J. H., et al., 2018, AJ, 156, 277

Luger R., Agol E., Foreman-Mackey D., Fleming D. P., Lustig-Yaeger J., Deitrick R., 2019, aj, 157, 64

Lundkvist M. S., et al., 2016, Nature Communications, 7, 11201

Maciejewski G., et al., 2016, A&A, 588, L6

Madhusudhan N., Winn J. N., 2009, ApJ, 693, 784

Magliano C., et al., 2023, MNRAS, 519, 1562

Mamajek E. E., Hillenbrand L. A., 2008, ApJ, 687, 1264

Maxted P. F. L., et al., 2011, PASP, 123, 547

Mazeh T., Holczer T., Faigler S., 2016, A&A, 589, A75

McCully C., Volgenau N. H., Harbeck D.-R., Lister T. A., Saunders E. S., Turner M. L., Siiverd R. J., Bowman M., 2018, in Guzman J. C., Ibsen J., eds, Society of Photo-Optical Instrumentation Engineers (SPIE) Conference Series Vol. 10707, Software and Cyberinfrastructure for Astronomy V. p. 107070K (arXiv:1811.04163), doi:10.1117/12.2314340

Morton T. D., Bryson S. T., Coughlin J. L., Rowe J. F., Ravichandran G., Petigura E. A., Haas M. R., Batalha N. M., 2016, ApJ, 822, 86

Namouni F., Morais H., 2017, arXiv e-prints, p. arXiv:1704.00550

Noyes R. W., Weiss N. O., Vaughan A. H., 1984, ApJ, 287, 769

Ogihara M., Hori Y., Kunitomo M., Kurosaki K., 2021, A&A, 648, L1

Ogilvie G. I., 2014, ARA&A, 52, 171

Otegi J. F., Bouchy F., Helled R., 2020, A&A, 634, A43

Owen J. E., Lai D., 2018, MNRAS, 479, 5012

Patra K. C., Winn J. N., Holman M. J., Yu L., Deming D., Dai F., 2017, AJ, 154, 4

Patra K. C., et al., 2020, AJ, 159, 150

Pecaut M. J., Mamajek E. E., 2013, ApJS, 208, 9

Pepe F., et al., 2002, The Messenger, 110, 9

Persson C. M., et al., 2022, A&A, 666, A184

Piskunov N., Valenti J. A., 2017, A&A, 597, A16

Piso A.-M. A., Youdin A. N., Murray-Clay R. A., 2015, ApJ, 800, 82

Pollacco D. L., et al., 2006, PASP, 118, 1407

Pollack J. B., Hubickyj O., Bodenheimer P., Lissauer J. J., Podolak M., Greenzweig Y., 1996, Icarus, 124, 62

Ricker G. R., et al., 2015, Journal of Astronomical Telescopes, Instruments, and Systems, 1, 014003

Ryabchikova T., Pakhomov Y., 2015, Baltic Astronomy, 24, 453

Salvatier J., Wiecki T. V., Fonnesbeck C., 2016, PeerJ Computer Science, 2, e55

Sanchis-Ojeda R., Rappaport S., Winn J. N., Kotson M. C., Levine A., El Mellah I., 2014, ApJ, 787, 47

Santos N. C., et al., 2013, A&A, 556, A150

Santos N. C., et al., 2015, A&A, 580, L13

Santos N. C., et al., 2017, A&A, 608, A94

Schlegel D. J., Finkbeiner D. P., Davis M., 1998, ApJ, 500, 525

Scott N. J., et al., 2021, Frontiers in Astronomy and Space Sciences, 8, 138

Skrutskie M. F., et al., 2006, AJ, 131, 1163

Smith J. C., et al., 2012, PASP, 124, 1000

Sneden C. A., 1973, PhD thesis, University of Texas, Austin

Sousa S. G., 2014, in , Determination of Atmospheric Parameters of B. Springer, pp 297–310, doi:10.1007/978-3-319-06956-2_26

Sousa S. G., Santos N. C., Israelian G., Mayor M., Monteiro M. J. P. F. G., 2007, A&A, 469, 783

Sousa S. G., et al., 2008, A&A, 487, 373

Sousa S. G., Santos N. C., Adibekyan V., Delgado-Mena E., Israelian G., 2015, A&A, 577, A67

Sousa S. G., et al., 2021, A&A, 656, A53

Stassun K. G., Torres G., 2016, AJ, 152, 180

Stassun K. G., Torres G., 2021, ApJ, 907, L33

Stassun K. G., Collins K. A., Gaudi B. S., 2017, AJ, 153, 136

Stassun K. G., Corsaro E., Pepper J. A., Gaudi B. S., 2018, AJ, 155, 22

Stassun K. G., et al., 2019, AJ, 158, 138

Strugarek A., Bolmont E., Mathis S., Brun A. S., Réville V., Gallet F., Charbonnel C., 2017, ApJ, 847, L16

Stumpe M. C., et al., 2012, PASP, 124, 985

Stumpe M. C., Smith J. C., Catanzarite J. H., Van Cleve J. E., Jenkins J. M., Twicken J. D., Girouard F. R., 2014, PASP, 126, 100

Szabó G. M., Kiss L. L., 2011, ApJ, 727, L44

Theano Development Team 2016, arXiv e-prints, abs/1605.02688

Torres G., Andersen J., Giménez A., 2010, A&ARv, 18, 67

Triaud A. H. M. J., 2018, in Deeg H. J., Belmonte J. A., eds, , Handbook of Exoplanets. Springer, p. 2, doi:10.1007/978-3-319-55333-7_2

Twicken J. D., Chandrasekaran H., Jenkins J. M., Gunter J. P., Girouard F., Klaus T. C., 2010, in Radziwill N. M., Bridger A., eds, Society of Photo-Optical Instrumentation Engineers (SPIE) Conference Series Vol. 7740, Software and Cyberinfrastructure for Astronomy. p. 77401U, doi:10.1117/12.856798

Twicken J. D., et al., 2018, PASP, 130, 064502

Valenti J. A., Piskunov N., 1996, A&AS, 118, 595

Vehtari A., Gelman A., Simpson D., Carpenter B., Bürkner P.-C., 2021, Bayesian Analysis, 16, 667

Vick M., Lai D., 2018, MNRAS, 476, 482

Vick M., Lai D., Anderson K. R., 2019, MNRAS, 484, 5645

Vissapragada S., et al., 2022, AJ, 164, 234

West R. G., et al., 2019, MNRAS, 486, 5094

Winn J. N., et al., 2010, ApJ, 723, L223

Winn J. N., Sanchis-Ojeda R., Rappaport S., 2018, New Astron. Rev., 83, 37

Wong I., Shporer A., Vissapragada S., Greklek-McKeon M., Knutson H. A., Winn J. N., Benneke B., 2022, AJ, 163, 175

Wu Y., 2018, AJ, 155, 118

Yee S. W., et al., 2020, ApJ, 888, L5

APPENDIX A: PHOTOMETRY

The full set of six transits from LCOGT described in Section 2.1.2 are shown in Fig. A1. The PEST transit described in Section 2.1.3 is shown in Fig. A2. Described in Section 2.1.4, the phase folded WASP data are shown in Fig. A3, and the periodograms from each of the four different years of WASP data are shown in Fig. A4.

APPENDIX B: SPECTROSCOPY

The HARPS RV data (described in Section 2.2.1) are presented in Table B1.

APPENDIX C: SPECTROSCOPIC ANALYSIS AND CHEMICAL ABUNDANCES

Stellar abundances determined by the methods outlined in Section 3 are presented in Table C1. The spectral energy distribution used for determining stellar parameters in Section 3 is shown in Fig. C1.
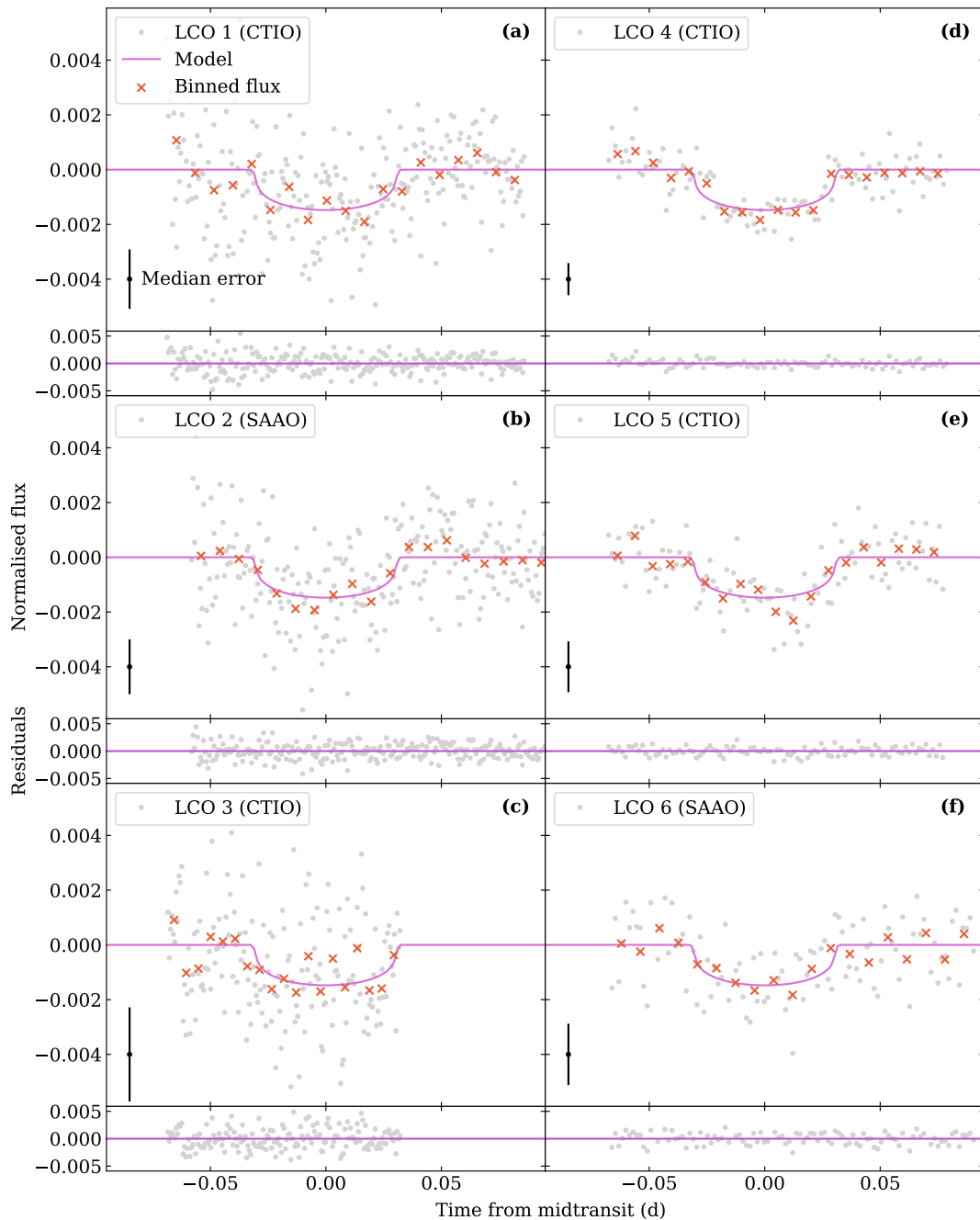
APPENDIX D: THE JOINT FIT

The full set of priors and fit values from our joint fit model described in Section 4 are presented in Table D1.

APPENDIX E: CO-ORBITAL BODIES

The full set of priors and posteriors from each of the four co-orbital scenario models described in Section 5.2 are presented in Table E1.
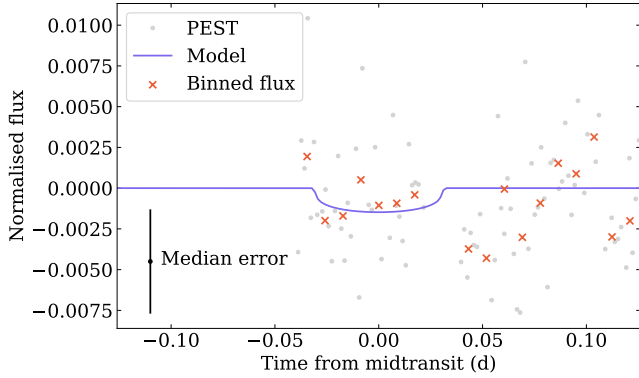
Figure A1. Photometric data from LCOGT. For each, the flux (grey circles), binned flux (red crosses), median error on the flux (one standard deviation, black error bar, bottom left) and best fit model (solid line) are shown. Residuals after the best fit model is subtracted are shown in the bottom panels. Data were captured at two different telescopes in the Global Network, the Cerro Tololo Inter-American Observatory (CTIO) and the South African Astronomical Observatory (SAAO), on the nights of:

(a) 1 June 2019 at CTIO in Sloan i' band ("LCO 1");

(b) 10 July 2019 at SAAO in Sloan i' band ("LCO 2");

(c) 27 July 2019 at CTIO Pan-STARRS z-short band ("LCO 3");

(d) 10 Aug 2019 at CTIO in Sloan g' band ("LCO 4");

(e) 10 Aug 2019 at CTIO in Pan-STARRS z-short band ("LCO 5");

and **(f)**, 24 Aug 2020 at SAAO in Pan-STARRS z-short band ("LCO 6").

Table B1. HARPS radial velocities.

| Time (RJD)	RV (ms^{-1})	σ_{RV} (ms^{-1})	FWHM (ms^{-1})	Bisector (ms^{-1})	Contrast
59544.57860093983	-6694.929826	2.367355	6392.280263	26.740961	46.535725
59545.55694768019	-6649.202052	2.955035	6388.488003	25.186455	46.576300
59547.619848280214	-6715.203341	3.033317	6385.913640	18.836766	46.524531
59548.59424903989	-6657.213721	2.254944	6393.227848	23.858339	46.540726
59549.57656604005	-6671.028545	2.193774	6382.831911	13.896637	46.601883
59550.5969126299	-6731.050809	3.426731	6391.442681	32.262988	46.546534
59573.55401741015	-6649.345311	2.595591	6395.329891	10.285248	46.332886
59574.5364167802	-6692.040443	3.867689	6385.126449	19.361261	45.940802
59578.54254523991	-6732.742673	4.000978	6394.998608	29.815993	46.371621
59580.54742026003	-6650.166676	3.263565	6384.294121	3.673344	46.562577
59581.54694268014	-6711.154291	5.927420	6393.494683	34.206176	46.592209
59582.541859869845	-6732.443878	2.576812	6378.507589	10.085069	46.563025
59726.90363577986	-6723.985683	2.841378	6385.428239	13.959675	46.604519
59727.8527730098	-6731.586132	2.598389	6379.880003	21.284249	46.570771
59728.80604236014	-6672.012893	3.704808	6385.685635	36.586262	46.578561
59728.92009065999	-6655.110375	6.944427	6370.694975	26.775309	46.895611

The full HARPS data products can be found on ExoFOP-TESS at `https://exofop.ipac.caltech.edu/tess/target.php?id=139285832`

Figure A2. Photometric data from PEST (a single transit event), where the flux (grey circles), binned flux (red crosses), and median error on the flux (one standard deviation, black error bar, bottom left) are shown. This data was not included in our joint fit model (see Section 2.1.3), but we overplot the best fit model with a solid line.
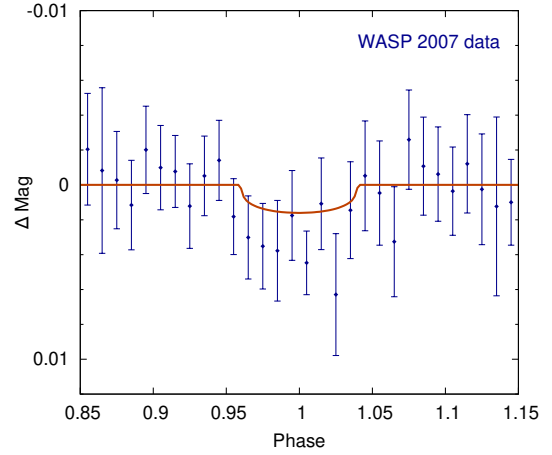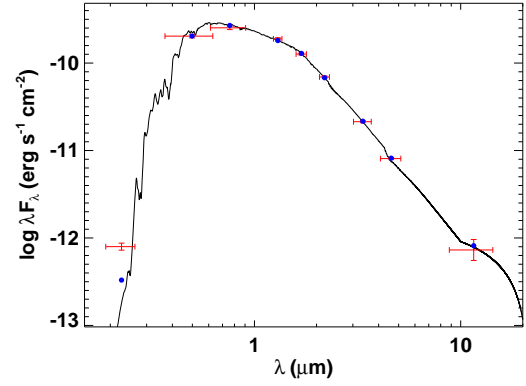

Figure A3. Photometric data from WASP (2007 data only), phase-folded on the transit ephemeris. This data was not included in our joint fit model (see Section 2.1.4), but we overplot the best fit model with a solid line.
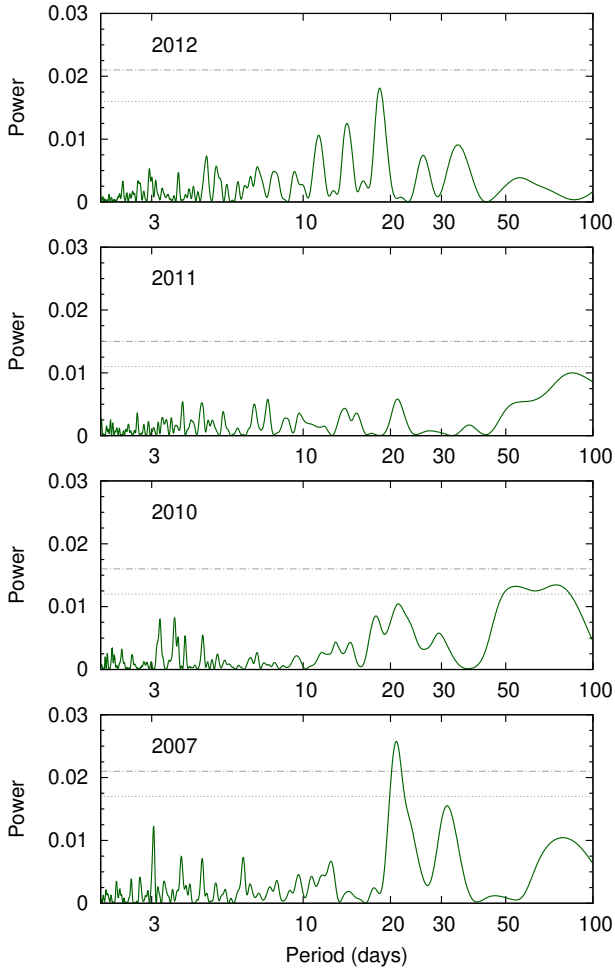
Figure A4. Periodograms of the WASP-South data for TOI-332 from four different years of data. The horizontal lines mark the estimated 10 per cent- and 1 per cent-likelihood false-alarm levels. A significant periodicity at 20.9± 1.0 d was seen in 2007.

Figure C1. Spectral energy distribution of TOI-332. Red symbols represent the observed photometric measurements, where the horizontal bars represent the effective width of the passband. Blue symbols are the model fluxes from the best-fit Kurucz atmosphere model (black).

Table C1. Stellar abundances determined by the methods outlined in Section 3.

Chemical abundances	Value (dex)
[Ca/H]	0.22 ± 0.06
[Na/H]	0.37 ± 0.07
[Mg/H]	0.26 ± 0.06
[Al/H]	0.34 ± 0.06
[Si/H]	0.24 ± 0.04
[Ti/H]	0.33 ± 0.06
[Ni/H]	0.27 ± 0.04
[O/H]	0.23 ± 0.15
[C/H]	0.22 ± 0.04
[Cu/H]	0.41 ± 0.09
[Zn/H]	0.25 ± 0.05
[Sr/H]	0.33 ± 0.17
[Y/H]	0.18 ± 0.11
[Zr/H]	0.18 ± 0.11
[Ba/H]	0.10 ± 0.09
[Ce/H]	0.20 ± 0.15
[Nd/H]	0.27 ± 0.08

Table D1. Prior distributions used in our joint fit model, fully described in Section 4, and the fit values resulting from the model. The priors are created using distributions in PyMC3 with the relevant inputs to each distribution described in the table footer. The fit values are given as the median values of the samples, and the uncertainties as the 16th and 84th percentiles. Further (derived) system parameters can be found in Table 2.

Parameter	(unit)	Prior Distribution	Fit value
Planet			
Period P	(days)	$\mathcal{U}(0.767, 0.787)$	0.777038 ± 0.000001
Reference time of midtransit t_c	(BJD-2457000)	$\mathcal{U}(2062.4439, 2062.4459)$	$2062.4447^{+0.0006}_{-0.0005}$
$\log(R_P)$	($R_\odot$)	$\mathcal{U}(-4.6863, -2.6863)^*$	$-3.53^{+0.05}_{-0.04}$
Eccentricity e		0 (fixed)	-
Argument of periastron ω	(°)	0 (fixed)	-
Star			
Mass $M_\star$	($M_\odot$)	$\mathcal{N}_\mathcal{B}(0.88, 0.02, 0.0, 3.0)$	0.88 ± 0.02
Radius $R_\star$	($R_\odot$)	$\mathcal{N}_\mathcal{B}(0.87, 0.03, 0.0, 3.0)$	$0.87^{+0.03}_{-0.02}$
Photometry			
$TESS_{S1,2}$ mean		$\mathcal{N}(0.0, 1.0)$	0.00006 ± 0.00001
$TESS_{S28}$ mean		$\mathcal{N}(0.0, 1.0)$	0.00008 ± 0.00002
LCO_1 mean		$\mathcal{N}(0.0, 1.0)$	0.00050 ± 0.00007
LCO_2 mean		$\mathcal{N}(0.0, 1.0)$	0.00049 ± 0.00007
LCO_3 mean		$\mathcal{N}(0.0, 1.0)$	0.0008 ± 0.0001
LCO_4 mean		$\mathcal{N}(0.0, 1.0)$	0.00051 ± 0.00006
LCO_5 mean		$\mathcal{N}(0.0, 1.0)$	0.00053 ± 0.00009
LCO_6 mean		$\mathcal{N}(0.0, 1.0)$	0.0005 ± 0.0001
HARPS RVs			
$\log(K)$		$\mathcal{U}(0.0, 10.0)$	3.77 ± 0.02
Offset	(m s^{-1})	$\mathcal{U}(-6702, -6682)$	-6692.4 ± 0.8
$\log$ (Jitter)		$\mathcal{N}(2.193774^\dagger, 5.0)$	$-1.1^{+1.1}_{-1.8}$

Distributions:

$\mathcal{N}(\mu, \sigma)$: a normal distribution with a mean μ and a standard deviation σ;

$\mathcal{N}_\mathcal{B}(\mu, \sigma, a, b)$: a bounded normal distribution with a mean μ, a standard deviation σ, a lower bound a, and an upper bound b (bounds optional);

$\mathcal{U}(a, b)$: a uniform distribution with a lower bound a, and an upper bound b.

Prior values:

* equivalent to $0.5(\log(D)) + \log(R_\star) \pm 1$ where D is the transit depth (ppm multiplied by 10^{-6}) and $R_\star$ is the mean of the prior on the stellar radius ($R_\odot$), and -1 computes the lower bound while $+1$ computes the upper bound;

† equivalent to the log of the minimum error on the HARPS data (m s^{-1}).

Table E1. Co-orbital hypothesis results.

Parameter	Priors	Posteriors			
		1p(c)	1p	1p(c)T	1pT
P (days)	$\mathcal{G}(0.77703817, 10^{-8})$	$0.77703792 \pm 9.9 \times 10^{-7}$	$0.77703812 \pm 9.9 \times 10^{-7}$	Fixed	Fixed
t_0 (BJD-2457000)	$\mathcal{G}(2062.444852864292, 4\times10^{-7})$	$2062.44496903 \pm 4 \times 10^{-7}$	$2062.44496903 \pm 4 \times 10^{-7}$	Fixed	Fixed
K_b (m s^{-1})	$\mathcal{U}(0.0, 100.0)$	$43.1^{+1.2}_{-1.2}$	$43.2^{+1.2}_{-1.2}$	$43.1^{+1.2}_{-1.2}$	$43.2^{+1.2}_{-1.2}$
e	$\mathcal{U}(0.0, 1.0)$	Circular	$0.025^{+0.021}_{-0.016}$	-	-
ω (deg.)	$\mathcal{U}(0.0, 359.99)$	Circular	215^{+38}_{-72}	-	-
c	$\mathcal{G}(0.0, 0.05)$	-	-	-	0.028 ± 0.025
d	$\mathcal{G}(0.0, 0.05)$	-	-	-	0.014 ± 0.026
δ_{HARPS} (km s^{-1})	$\mathcal{U}(-15.0, -0.0)$	$-6.69198^{+0.00091}_{-0.00088}$	$-6.69194^{+0.00088}_{-0.00088}$	$-6.69209^{+0.00091}_{-0.00089}$	$-6.69184^{+0.00091}_{-0.00090}$
σ_{HARPS} (m s^{-1})	$\mathcal{U}(0.0, 5.0)$	$1.6^{+1.3}_{-1.0}$	$1.33^{+1.3}_{-0.91}$	$1.5^{+1.4}_{-1.0}$	$1.4^{+1.4}_{-1.0}$
$\ln \mathcal{Z}$		55.5	52.7	48.9	48.4

Posteriors are given for the following models, as described in Section 5.2:

"1p(c)", one planet on a circular orbit;

"1p", one planet with the possibility of an eccentric orbit;

"1p(c)T", a co-orbital scenario with a circular orbit;

"1pT", a co-orbital scenario with the possibility of an eccentric orbit.

The period and time of conjunction posteriors coincide with the priors as they are much more constrained by the transit modelling. All posteriors for the systemic velocity agree within 1σ.

APPENDIX F: AUTHOR AFFILIATIONS

[1]Department of Physics, University of Warwick, Gibbet Hill Road, Coventry CV4 7AL, UK

[2]Centre for Exoplanets and Habitability, University of Warwick, Gibbet Hill Road, Coventry CV4 7AL, UK

[3]Institute for Computational Science, University of Zurich, Winterthurerstr. 90, 8057 Zurich, Switzerland

[4]Instituto de Astrofísica e Ciências do Espaço, Universidade do Porto, CAUP, Rua das Estrelas, 4150-762 Porto, Portugal

[5]Center for Astrophysics | Harvard & Smithsonian, 60 Garden Street, Cambridge, MA 02138, USA

[6]Department of Space, Earth and Environment, Chalmers University of Technology, Onsala Space Observatory, 439 92 Onsala, Sweden

[7]Astrophysics Group, Keele University, Staffordshire ST5 5BG, UK

[8]Astrophysics Research Centre, School of Mathematics and Physics, Queen's University Belfast, BT7 1NN Belfast, UK

[9]Department of Astronomy, University of Michigan, Ann Arbor, MI 48109, USA

[10]Centro de Astrobiología (CAB, CSIC-INTA), Depto. de Astrofísica, ESAC campus, 28692, Villanueva de la Cañada (Madrid), Spain

[11]U.S. Naval Observatory, Washington, D.C. 20392, USA

[12]Max Planck Institute for Astronomy, Heidelberg, Germany

[13]Departamento de Física e Astronomia, Faculdade de Ciências, Universidade do Porto, Rua do Campo Alegre, 4169-007 Porto, Portugal

[14]Department of Physics and Astronomy, Vanderbilt University, Nashville, TN 37235, USA

[15]Perth Exoplanet Survey Telescope

[16]Department of Physics and Kavli Institute for Astrophysics and Space Research, Massachusetts Institute of Technology, Cambridge, MA 02139, USA

[17]Department of Earth, Atmospheric and Planetary Sciences, Massachusetts Institute of Technology, Cambridge, MA 02139, USA

[18]Department of Aeronautics and Astronautics, MIT, 77 Massachusetts Avenue, Cambridge, MA 02139, USA

[19]Department of Astrophysical Sciences, Princeton University, Princeton, NJ 08544, USA

[20]NASA Ames Research Center, Moffett Field, CA 94035, USA

[21]Department of Astronomy, MC 249-17, California Institute of Technology, Pasadena, CA 91125, USA

[22]NASA Exoplanet Science Institute - Caltech/IPAC, Pasadena, CA USA

[23]George Mason University, 4400 University Drive, Fairfax, VA, 22030 USA

[24]NASA Goddard Space Flight Center, Exoplanets and Stellar Astrophysics Laboratory (Code 667), Greenbelt, MD 20771, USA

[25]International Center for Advanced Studies (ICAS) and ICIFI (CONICET), ECyT-UNSAM, Campus Miguelete, 25 de Mayo y Francia, (1650) Buenos Aires, Argentina

[26]ETH Zurich, Institute for Particle Physics and Astrophysics, Wolfgang-Pauli-Strasse 27, CH-8093 Zurich Switzerland

[27]Department of Astronomy of the University of Geneva, Geneva Observatory, Chemin Pegasi 51, 1290 Versoix, Switzerland

[28]Department of Astronomy and Tsinghua Centre for Astrophysics, Tsinghua University, Beijing 100084, China

[29]European Southern Observatory, Karl-Schwarzschild-Straße 2, 85748 Garching bei München, Germany

[30]Physikalisches Institut, University of Bern, Gesellsschaftstrasse 6, 3012 Bern, Switzerland

[31]South African Astronomical Observatory, P.O. Box 9, Observatory, Cape Town 7935, South Africa

[32]SETI Institute, Mountain View, CA 94043 USA

This paper has been typeset from a TEX/LATEX file prepared by the author.